SAND2023-14944J

Nonlinear analysis and vibro-impact characteristics of a shaft-bearing assembly

B. E. Saunders[1], R. J. Kuether [2], R. Vasconcellos[3], and A. Abdelkefi[1*]

[1]Deptartment of Mechanical & Aerospace Engineering, New Mexico State University, Las Cruces, NM 88003, USA.
[2]Sandia National Laboratories, Albuquerque, NM 87123, USA.
[3]São Paulo State University (UNESP), Campus of São João da Boa Vista, São João da Boa Vista 13876-750, Brazil.

Abstract

This study investigates the nonlinear frequency response of a shaft-bearing assembly with vibro-impacts occurring at the bearing clearances. The formation of nonlinear behavior as system parameters change is examined, along with the effects of asymmetries in the nominal, inherently symmetric system. The primary effect of increasing the forcing magnitude or decreasing the contact gap sizes is the formation of grazing-induced chaotic solution branches occurring over a wide frequency range near each system resonance. The system's nominal setup has very hard contact stiffness and shows no evidence of isolas or superharmonic resonances over the frequency ranges of interest. Moderate contact stiffnesses cause symmetry breaking and introduce superharmonic resonance branches of primary resonances. Even if some primary resonances are not present due to the system's inherent symmetry, their superharmonic resonances still manifest. Branches of quasiperiodic isolas (isolated resonance branches) are also discovered, along with a cloud of isolas near a high-frequency resonance. Parameter asymmetries are found to produce a few significant changes in behavior: asymmetric linear stiffness, contact stiffness, and gap size could affect the behavior of primary resonant frequencies and isolas.

Keywords: Nonlinear dynamics, contact/impact, isolas, stability, asymmetry

1. Introduction

Bearing-mounted shaft structures are common in gear drives and other mechanical engineering systems. Nonlinear phenomena including large or plastic deformations, friction, and intermittent contact between parts can occur during normal operation. The present work is interested in characterizing the resulting complex nonlinear dynamics which can occur in such shaft-bearing systems, specifically when the shaft is not rotating. Micro clearances within the bearings can lead to contact/impact nonlinearities, and other factors, such as base or forcing excitations [1], unbalance [2], and impacts caused by gear dynamics [3], can contribute to both vibrational and shock effects in the assembly. Bearing clearances coupled with a sinusoidal forcing causes intermittent contact and turns the structure into a vibro-impact system.

The techniques used to analyze systems in complex nonlinear environments include classical modal analysis [4], perturbation techniques [5], time integration [6], and finite element analysis [7]. While time integration methods can capture both nonlinear periodic and aperiodic behaviors, they often lack the ability to clearly resolve full solution branches which are easily computed with harmonic balancing methods [8]. Harmonic balance is in turn incapable of capturing aperiodic motions such as chaos. Well-known and classical methods like linear modal analysis do not hold for nonlinear systems unless the nonlinearity is weak and can be linearized with acceptable accuracy. Some nonlinearities, such as contact/impact, cannot be linearized easily or may only be linearized in certain limits as the contact gaps and stiffnesses become sufficiently large or small [9]. Contact behavior operating within these limits, and other effects such as large-amplitude vibrations and mechanical shock, all tend to cause strongly nonlinear responses, so approximations with linear modal analysis neglect extremely important behaviors. These behaviors may be desirable or undesirable depending on the application.

An example of beneficial nonlinear behavior is a clearance between moving parts designed to cause intermittent contact and the transfer of energy between the modes of the parts. This form of targeted energy transfer can mitigate the effects of mechanical shock. Gzal et al. [6] described an intermodal target energy transfer (IMTET) mechanism, which used impact constraints on a 2 degree of freedom (DOF) dynamical system and later on a 9 DOF building model [10] to transfer the system's energy from low-frequency modes to high-frequency modes during a shock excitation. They found that both elastic and inelastic impact led to more efficient utilization of the inherent damping in the system without the need to change mass, stiffness, or damping properties. On the other hand, an often-detrimental nonlinear behavior is the potential formation of isolated resonance branches, also known as isolas [11]. Isolas tend to be undesirable behavior since they are often difficult to detect, and a perturbation in a system can cause an unexpected jump from a low-amplitude response to a high-amplitude response. Isolas are dependent on forcing magnitude, allowing them to grow in their frequency range and even merge with the main branch of the frequency response as system parameters are varied. The above examples show that whether a given nonlinear behavior is desirable or not, an accurate solution method is nevertheless essential to properly characterize the various behaviors possible in a vibro-impact system. Even then, an efficient combination of two or more solution methods may further improve the clarity of the results.

Focusing on bearing-mounted systems, complex nonlinear dynamical behavior, including isola formation, has been researched over the years. A work by Ehrich et al. [12] studied a 2 DOF model of a rotor-stator system to assess the effect of bearing clearances on the system dynamics. They observed that larger bearing clearances lead to hardening behavior in the frequency response. Branches of stable

solutions that detached from the main response were also observed, which suggests the formation of isolas. Baguet et al. [13] studied a more complex gear drive with a gear, pinion, two shafts, and four journal bearings. Time-varying properties and nonlinearities in the gears and bearings with clearances were included. They found that the system motion is dominated by mesh excitations for high values of torque and by mass unbalance for low values of torque, but no isolas were observed. Gunduz et al. [14] analyzed the effects of bearing preloads in a vehicle wheel bearing assembly both analytically and experimentally. Increased preloads were found to shift the resonance frequencies and amplitudes. Both preload-independent and dependent damping models were also considered, which led to higher and lower amplitudes as the axial preload increased, respectively. The effects of axial and radial clearances were also included, but a nonlinear study of the clearances was omitted.

Ehehalt et al. [15] outlined an experimental approach to study a modular kit for rotordynamic experiments with rotor-stator contact. They presented several sets of single DOF and multiple DOF experimental results and discussed the various types of nonlinear behaviors which appeared including stator whirl, super- and sub-harmonic motions, quasiperiodic motions, chaos, modal interactions, and isolas. Experimental results used a wide variety of bearings: ball, journal, active magnetic, retainer, and elastic bearings. Xu et al. [3] studied a 14 DOF gear-shaft-bearing-housing vibration model to understand the effects of vibration caused by progressively larger bearing clearances. They proposed a modulation signal bispectrum-sideband estimator, MSB-SE, as a wear indicator. The authors extended their work to a two-stage spur gearbox which was run until failure. Molaie et al. [16] developed an SDOF model of a spiral bevel gear system accounting for backlash, tooth-profile manufacturing errors, teeth spacing errors, and tooth elastic deformation. They observed both softening and hardening behavior in the frequency response, along with chaos. Increased backlash led to an increase in vibration amplitudes, and increased damping reduced the overall vibration amplitude but could lead to chaos and subharmonic resonances. Chen et al. [17] applied a modified harmonic balance and alternating frequency/time method to the analysis of a dual-rotor-bearing-casing system with 284 DOFs. Frequency hardening and the accompanying hysteresis behavior were present, but isolas were not observed. As bearing clearance was increased, softening behavior occurs and causes a wider hysteresis region.

For completeness, a superharmonic resonance occurs when a nonlinearity causes a significant growth in a system's response amplitude at a frequency below its primary resonance frequency, usually an integer fraction. When the frequency content of that individual solution is observed, e.g. via Fast Fourier Transform (FFT), then spikes will be seen at integer-multiple frequencies above the system's primary resonant frequency. This can be confusing because there are two separate frequency spectra:

that of the system's response, and that of individual responses. Subharmonic resonances are the opposite of superharmonic resonances: high amplitudes at a response frequency above the primary resonance frequency, whose time history has frequency content below the primary resonance frequency. Isolated resonances, or isolas, often occur as subharmonic resonances.

The study of isolas is important because they have implications for the performance and lifetime of engineering components. Researchers have discovered and observed many systems in which isolas can be present near the primary resonances of the system. If these isolas vary with system parameters and merge with the main resonance, then the resonance amplitude and frequency can significantly and suddenly shift in value. A leading cause for isola formation is hypothesized to be the interaction between different nonlinear normal modes, and this has been observed both numerically [11, 18, 19] and experimentally [7, 20, 21]. The strong nonlinearity that gives rise to isolas also tends to promote additional nonlinear behaviors as well. Habib et al. [22] developed a nonlinear tuned vibration absorber (NLTVA) which, despite having superior qualities to a linear vibration absorber, could not prevent an isola forming around the primary system resonance along with quasiperiodic motions. Shaw et al. [7] experimentally studied a cantilever beam with variable nonlinear tip spring. The system exhibited a 3:1 internal resonance, frequency hardening, isolas, quasiperiodic motion with Neimark-Sacker bifurcations, and other dynamical behaviors. Hong et al. [23] studied the conditions under which isolas can form in a nonlinear tuned mass damper and found symmetry-breaking to play an important role in system dynamics. Isolas can also form far away from primary resonances where they are not expected, for example near ultra-subharmonic resonances [24, 25] or at amplitudes below the main frequency response branch [26, 27]. Furthermore, the presence of contact behavior in a system that also has other nonlinearities has been found to accelerate the formation of various nonlinear behaviors, including subharmonic and ultra-subharmonic isolas [28].

The above works mentioned the existence of chaotic motions, super- and sub-harmonic resonances, hysteretic jump phenomenon, quasiperiodic motions, isolas, and other well-known nonlinear behaviors [29]. The possibility of such behavior controls the design of a system, influences prediction of fatigue life, and even governs the type of simulation methods used to model the system. The objective of this paper is to investigate the complex nonlinear dynamic behavior of a non-rotating bearing-mounted structure with known clearances within the bearings. The bearing clearances turn the otherwise linear system into a vibro-impact system. Such systems are strongly influenced by the piecewise linear behavior of the contacting components and asymmetries in the system and can lead to complexity when characterizing the system's dynamics. The structure of interest is the experimental system introduced in Goldberg et al. [30], in which an idealized shaft-bearing assembly was designed to allow for

variations in the system configurations, including suspension and contact stiffness, contact gaps, mass, and asymmetry. A three degree-of-freedom (DOF) model is developed and parameterized with respect to these design variables, and the dynamics are studied using the computation of the nonlinear forced response curves. By leveraging both time integration methods and the multi-harmonic balance method (MHB), the complex behavior is more clearly described and uncovered, allowing for preliminary predictions of the experimental setup. The goal of this work is to investigate the formation of nonlinear behaviors, such as isolas or other secondary resonances, with respect to the test setup parameters such as contact stiffness and gap sizes. In addition, this study explores the effects of asymmetries in the system, such as unequal stiffnesses or gap sizes at the locations subject to contact.

The remainder of the paper is structured as follows. Section 2 introduces the system of interest and its simplified model, along with the numerical methods used to simulate the system response. Section 3 presents a modal analysis of the linearized system in order to understand the fundamental behavior of the natural frequencies and mode shapes in both symmetric and asymmetric configurations. Sections 4 through 7 present results showing the effects of several important parameters of the nonlinear system, namely, forcing magnitude, contact gap size, contact stiffness, and damping. Section 8 presents nonlinear analyses of asymmetric system configurations and highlights trends of behavior also observed in the symmetric configuration. Lastly, Section 9 summarizes the analyses with conclusions.

2. System formulation and numerical methods

A bearing-and-shaft assembly is studied in this work, continuing the research of Goldberg et al. [30]. Their experimental setup consists of a beam ("impact beam") representing a non-rotating shaft, with the contact effects of the bearing clearances represented by impact hammer tips. The impact tips are designed to have variable gap heights through rotation of the threaded rods, while different impact stiffnesses are achieved through different impact hammer tips installed on the load cell. Compression springs on both ends are used to hold the impact beam within a box frame and are meant to represent soft suspension springs such that the lowest frequency modes imitate those of pseudo rigid body modes. The impact tips are also mounted to the frame structure. The center of the beam can be excited directly with a stinger via a hole in the bottom center of the box frame, or directly on the box frame itself. Fig. 1 shows a CAD image detailing the impact beam and full assembly. Goldberg et al. [30] demonstrated that the beam's response and the natural frequencies, overall, were "highly accurate" between the model and the test.

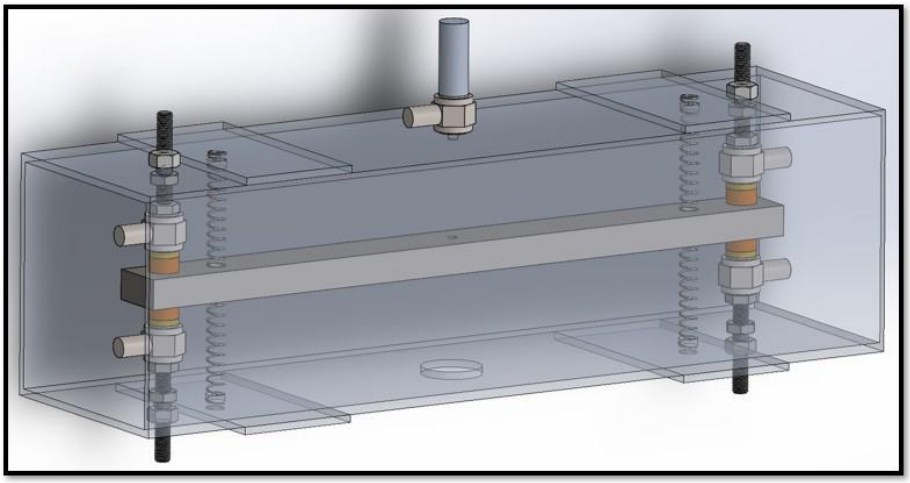

Fig. 1: The experimental box frame, impact tips, and impact beam assembly representing a non-rotating, bearing-supported shaft.

The shaft-bearing assembly under consideration is analyzed as a three degree-of-freedom system, as seen in Fig. 2. The impact beam's bending stiffness is included as a torsional spring, and the bearing impact effects are included as contact springs on the left and right DOFs, namely x_1 and x_3. The contact springs on a DOF only contribute to the system when the displacement of the DOF exceeds the contact gap. This behavior results in a piecewise-smooth force on the two DOFs. Contact damping was neglected in the original study [30] and is also neglected in the present work. Dissipation effects were included for some of the analyses in [30] in the form of a linear viscous damper applied equally to each DOF. A parameterized model is developed in this work by considering that the linear stiffnesses and contact parameters on DOFs x_1 and x_3 could be unequal and therefore make the system asymmetric, and by applying a harmonic forcing to any of the DOF. However, the nominal results are obtained for the symmetric system in which the parameters on DOFs x_1 and x_3 are identical, and for only a mono-harmonic excitation applied to the central DOF x_2, unless otherwise stated. It is noted that the model neglects the effects of gravity. Using Euler-Lagrange principle, the resulting simplified model is a nonlinear spring-mass system with the following equations of motion, given in matrix form and expanded form:

$$\mathbf{M}\ddot{\mathbf{x}} + \mathbf{C}\dot{\mathbf{x}} + \mathbf{K}\mathbf{x} + \mathbf{f}_{nl}(\mathbf{x}) = \mathbf{f}\cos(\omega t) \qquad (1a)$$

$$\begin{bmatrix} m_1 & 0 & 0 \\ 0 & m_2 & 0 \\ 0 & 0 & m_3 \end{bmatrix} \begin{bmatrix} \ddot{x}_1 \\ \ddot{x}_2 \\ \ddot{x}_3 \end{bmatrix} + \begin{bmatrix} c & 0 & 0 \\ 0 & c & 0 \\ 0 & 0 & c \end{bmatrix} \begin{bmatrix} \dot{x}_1 \\ \dot{x}_2 \\ \dot{x}_3 \end{bmatrix} + \begin{bmatrix} 2k_{s1} + \frac{\kappa}{L^2} & \frac{-2\kappa}{L^2} & \frac{\kappa}{L^2} \\ \frac{-2\kappa}{L^2} & \frac{4\kappa}{L^2} & \frac{-2\kappa}{L^2} \\ \frac{\kappa}{L^2} & \frac{-2\kappa}{L^2} & 2k_{s3} + \frac{\kappa}{L^2} \end{bmatrix} \begin{bmatrix} x_1 \\ x_2 \\ x_3 \end{bmatrix}$$

$$+ \begin{bmatrix} f_{g1}(x_1) \\ 0 \\ f_{g3}(x_3) \end{bmatrix} = \begin{bmatrix} p_1 \\ p_2 \\ p_3 \end{bmatrix} \cos(\omega t) \qquad (1b)$$

$$f_{gi}(x_i) = \begin{cases} k_{gi}(x_i + g_i), & x_i < -g_i \\ 0, & -g_i \le x_i \le g_i, \\ k_{gi}(x_i - g_i), & x_i > g_i \end{cases} \qquad i = 1,3 \qquad (1c)$$

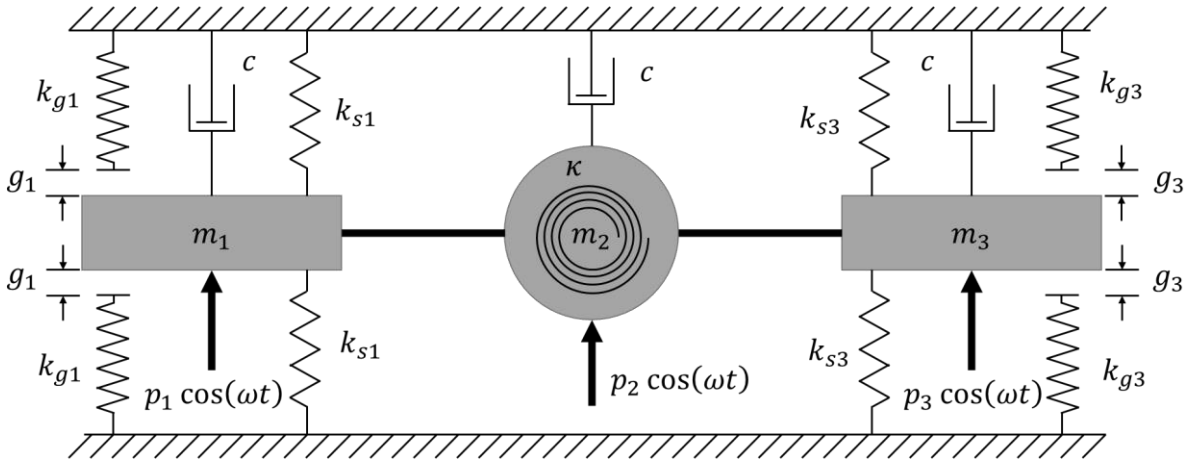

Fig. 2: Reduced-order model of the shaft-bearing assembly.

Table 1 lists the parameter values used in [30] and subsequently in this work. When the system is symmetric, $k_{s1} = k_{s3} = k_s, k_{g1} = k_{g3} = k_g$, and $g_1 = g_3 = g$. Also, the mass is distributed such that $m_1 = m_3 = m$ and $m_2 = 2m$.

Table 1: Default parameter values for the shaft-bearing model [30].

Description	Symbol	Value
Suspension spring stiffness	k_s	$8.03e3\ N/m$
Torsional spring stiffness	κ	$79161\ N*m/rad$
Gap spring stiffness	k_g	$3.502e7\ N/m$
Half-length	L	$0.1614\ m$
Gap	g	$2.54e-4\ m$
Left mass	m_1	$0.629\ kg$
Middle mass	m_2	$1.258\ kg$
Right mass	m_3	$0.629\ kg$
Damping coefficient	c	$4\ N*s/m$

Numerical simulations are performed in two ways. The first method is numerical time integration, specifically the MATLAB® *ode45* solver with the *Event Location* feature active [31, 32]. Each time

integration is started from a random initial condition (IC) from a range of realistic values. The integration time is chosen to be long enough for the transient-solution component to decay and allow the system to settle onto one attractor. This method distinguishes periodic, quasiperiodic, and chaotic motions, in addition to revealing the presence of multi-stable behavior by overlaying the results of multiple simulations. Fig. 3 is an example diagram of this *ode45*/Event Location scheme in order to show how the simulation behaves as a solution passes between in-contact and out-of-contact time domains. The black dashed lines mark the location of contacting springs; no contact occurs within this region, except at the boundaries where the solution can move into or out of contact. Near these points, mathematical expressions (such as those in Equation (1c)) are checked for sign changes which indicate the boundary has been crossed. *Ode45* activates a root finder to accurately locate the crossing, and the initial conditions are re-set to that point before the simulation starts again.

The second simulation method utilizes a harmonic balance solver formulated for nonlinear systems, the details of which are given by Colaïtis et al. [33]. This method captures the entirety of periodic solution branches and allows for Floquet stability analysis as a byproduct of the continuation scheme [33, 34]. This solver provides accurate results for systems with soft to moderately hard contact [35].

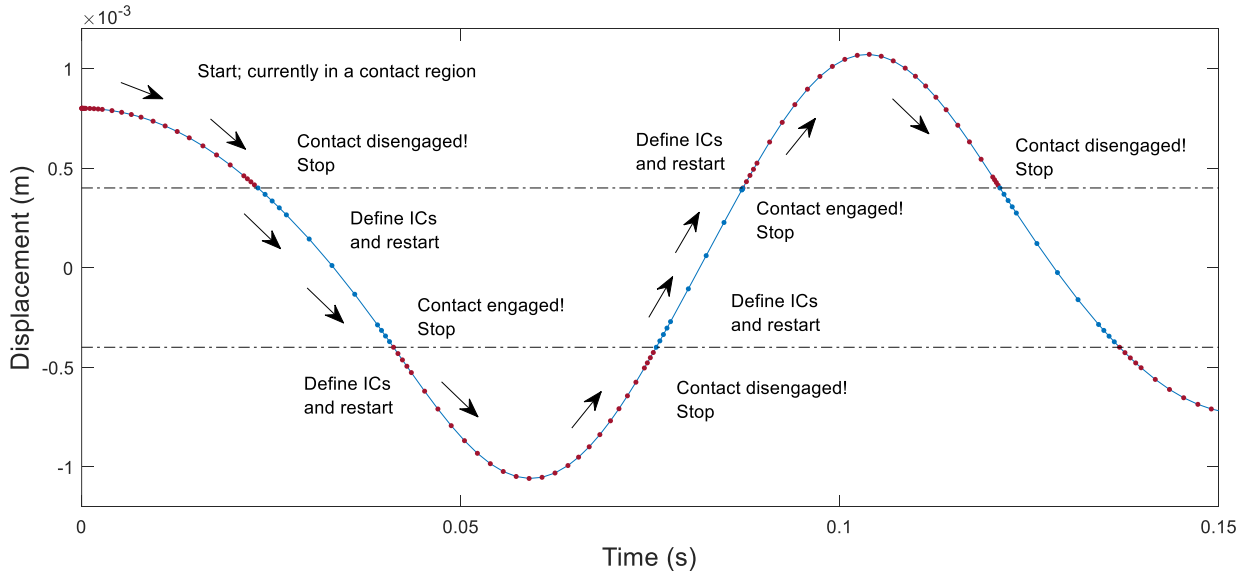

Fig. 3: Example diagram of the *ode45*/Event Location scheme.

The frequency response curves (FRC) are used to plot the results of the simulations, in which the maximum of the steady-state response is plotted with respect to forcing frequency and oftentimes a second parameter, such as gap size or forcing amplitude, for example. These plots are shown in both 2D and 3D forms, depending on which way provides clearer visualization of the results. Several isolas are encountered in the vibro-impact system's response and are detected by running multiple time

integrations from random ICs and overlaying the results in each plot. For harmonic balance results, isola continuation is initiated by first obtaining a time-integration solution on the isola and then curve-fitting a Fourier series to each DOF response. The resulting Fourier coefficients are then used as the initial guess. There is ongoing research on how to effectively detect isolas and other solutions besides the system's main solution branch [36, 37]. A more robust approach to discover isolas is beyond the scope of this work, but it remains an interesting topic for the research community.

3. Linearized analysis: system characteristics and asymmetry effects

3.1. Symmetric configuration

A first step in exploring the dynamics of the system is to calculate the linear undamped modes to serve as a reference to the forthcoming nonlinear results. Using eigenvalue analysis for the linear undamped system, the analytical natural frequencies and mode shapes of the shaft-bearing assembly in its nominal, symmetric configuration are as follows:

$$\omega_{1,2,3} = \omega_0\sqrt{\gamma-1}, \omega_0\sqrt{\frac{\gamma+3\pm\sqrt{\gamma^2-2\gamma+17}}{2}} \tag{3a}$$

$$\boldsymbol{X}_1 = \begin{bmatrix} 1 \\ \frac{\gamma-5+\alpha}{\gamma+3-\alpha} \\ 1 \end{bmatrix}, \boldsymbol{X}_2 = \begin{bmatrix} 1 \\ 0 \\ -1 \end{bmatrix}, \boldsymbol{X}_3 = \begin{bmatrix} 1 \\ \frac{\gamma-5-\alpha}{\gamma+3+\alpha} \\ 1 \end{bmatrix}, \tag{3b}$$

where $\omega_0 = \sqrt{\frac{\kappa}{mL^2}}, \gamma = \frac{2k_sL^2}{k} + 1$, and $\alpha = \sqrt{\gamma^2-2\gamma+17}$.

The nominal system values shown in Table 1 result in the following natural frequencies and magnitude-normalized linear normal modes of vibration:

$$\omega_1 \approx 17.9\,Hz, \omega_2 \approx 25.4\,Hz, \omega_3 \approx 699.9\,Hz, \tag{4a}$$

$$\widehat{\boldsymbol{X}}_1 \approx \frac{\sqrt{3}}{3}\begin{bmatrix} 1 \\ 1 \\ 1 \end{bmatrix}, \widehat{\boldsymbol{X}}_2 = \frac{\sqrt{2}}{2}\begin{bmatrix} 1 \\ 0 \\ -1 \end{bmatrix}, \widehat{\boldsymbol{X}}_3 \approx \frac{\sqrt{3}}{3}\begin{bmatrix} 1 \\ -1 \\ 1 \end{bmatrix} \tag{4b}$$

The first two modes of the system under investigation represent the pseudo rigid body modes due to the impact beam being suspended by soft support springs. These relate to a translational mode (all DOF translating in unison) or rotational mode (rotating about the center node). The first two natural frequencies are close in magnitude and are well separated from the third mode. The third mode of the system represents the fundamental bending mode of the impact bar in free-free boundary conditions where the middle node is moving out-of-phase with the two end nodes.

By taking the usual transformation with modal coordinates, the analytical solution to the forced undamped system can be obtained:

$$x_1(t) = \mathrm{X}_{11}\frac{p_1^*}{\omega^2-\omega_1^2}\cos(\omega t) + \mathrm{X}_{12}\frac{p_2^*}{\omega^2-\omega_2^2}\cos(\omega t) + \mathrm{X}_{13}\frac{p_3^*}{\omega^2-\omega_3^2}\cos(\omega t), \tag{5a}$$

$$x_2(t) = \mathrm{X}_{21}\frac{p_1^*}{\omega^2-\omega_1^2}\cos(\omega t) + \mathrm{X}_{22}\frac{p_2^*}{\omega^2-\omega_2^2}\cos(\omega t) + \mathrm{X}_{23}\frac{p_3^*}{\omega^2-\omega_3^2}\cos(\omega t), \quad (5b)$$

$$x_3(t) = \mathrm{X}_{31}\frac{p_1^*}{\omega^2-\omega_1^2}\cos(\omega t) + \mathrm{X}_{32}\frac{p_2^*}{\omega^2-\omega_2^2}\cos(\omega t) + \mathrm{X}_{33}\frac{p_3^*}{\omega^2-\omega_3^2}\cos(\omega t) \quad (5c)$$

where X_{ij} denotes the j^{th} component of the i^{th} mode shape, ω_i the i^{th} natural frequency, and p_j^* the j^{th} generalized forcing. As observed by the modes of the linear symmetric system, when the forced excitation is applied to the middle DOF, the second mode of the system does not get excited. For the full nonlinear system, therefore, the second resonance will only be activated via modal interaction resulting from the nonlinear contact force.

The above results are valid for the system with a fully open gap $g \gg 0$ large enough that contact never occurs. Fig. 4 shows the relationship between the contact stiffness, when the gap is fully closed ($g = 0$), and the linear undamped natural frequencies and mode shapes. The contact is continuous in this configuration, and so intermittent contact due to vibration still does not occur. Herrera et al. [9] indicate that these two extremes of the contact spectrum act as limiting behaviors, such that the system with an open gap (for which intermittent contact, and therefore nonlinear behaviors, can occur) will respond in some manner between these limiting behaviors. These results are obtained by appropriately adding the contact stiffness k_g to the system's stiffness matrix and performing an eigenvalue analysis. The results highlight the limiting behavior of the system, since the configurations with both a fully open gap and a fully closed gap are linear regardless the value of k_g, and both configurations coincide when $k_g = 0$ regardless the value of g. The closed-gap natural frequencies at the nominal contact stiffness are listed in Table 2 to be 451.1 Hz, 1188.0 Hz, and 1303.0 Hz, which agrees with the limiting behavior of the nonlinear modal analysis performed by Goldberg et al. [30]. Table 2 also lists the frequencies in the limiting cases of soft and hard contact stiffness. As $k_g \to \infty$, the lowest natural frequency approaches 494.7 Hz, and the higher two frequencies converge onto each other and grow proportionally to $k_g^{1/2}$. The corresponding mode shapes consist of two bending modes and one rotational mode. In this limit of contact stiffness, DOFs x_1 and x_3 become fixed boundary conditions with zero amplitude, and only x_2 is able to move in the first mode shape. The second mode shape (rotational) is unaffected by the change in contact stiffness, and the third mode shape (bending) remains a bending mode, but with zero motion at the middle node.

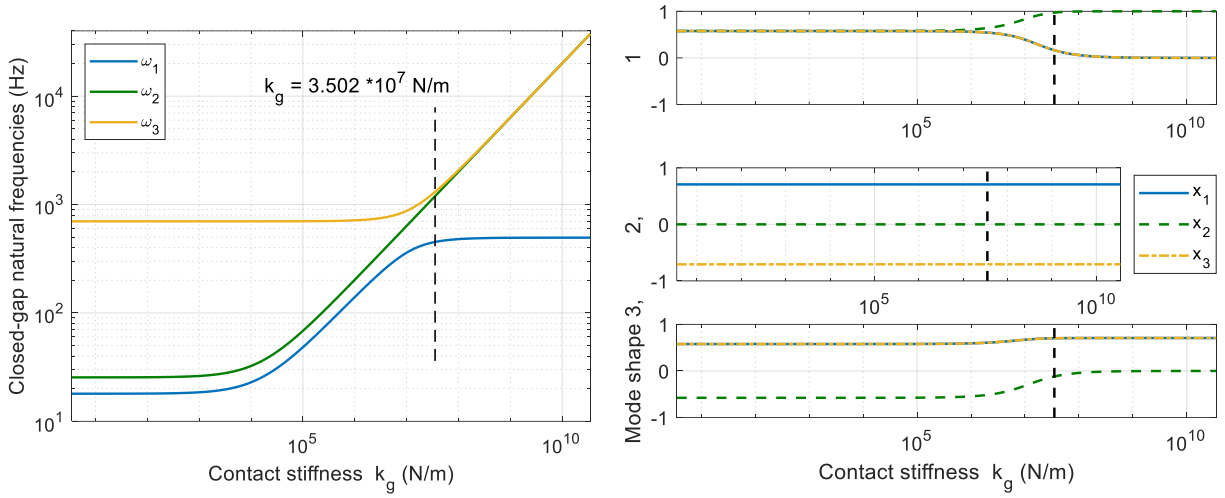

(a) (b)

Fig. 4: Linear undamped (a) natural frequencies and (b) mode shapes as a function of contact stiffness when the contact gap is fully closed $g = 0$. The vertical dashed line denotes the nominal contact stiffness $k_g = 3.502 * 10^7 N/m$ from Table 1.

Table 2: Natural frequencies at the nominal value and limiting values of contact stiffness.

k_g (N/m)	ω_1 (Hz)	ω_2 (Hz)	ω_3 (Hz)
$3.502 * 10^1$	18.0	25.4	699.9
$3.502 * 10^7$	451.1	1,180	1,303
$3.502 * 10^{10}$	494.7	37,560	37,560

3.2. Asymmetric configuration

For the linear system without contact, the system can lose symmetry if the linear springs on either side have different stiffnesses. If the x_1 linear stiffness is held fixed at k_s from Table 1 and the x_3 linear stiffness varies on the range $k_{s3} \in [0, k_s]$, then the results in Fig. 5 are obtained for the natural frequencies and mode shapes. The first natural frequency is found to vary in proportion to $k_s^{1/2}$ and decreases to zero as the asymmetry intensifies. The second natural frequency decreases a small amount from 25.43 Hz to 22.02 Hz, and the third natural frequency decreases negligibly. Table 3 lists the natural frequencies at the low and high limits shown in the figures. The breaking of symmetry due to the suspension spring, k_{s3}, causes the first two modes to no longer behave as purely translational and rotational pseudo-rigid body modes. This results in each mode mixing to both have a combination of rotation and translation about the central DOF as $k_{s3} \to 0$. The third mode shape is negligibly affected and remains a fundamental bending mode of the impact beam.

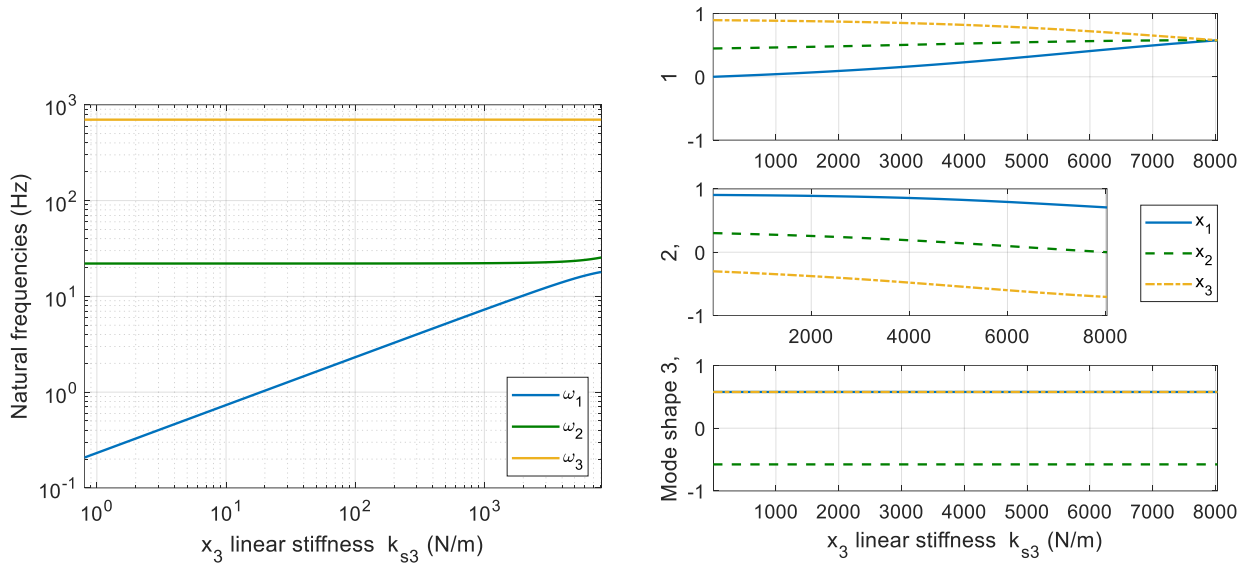

(a) (b)

Fig. 5: (a) Linear natural frequencies and (b) mode shapes as functions of the linear stiffness on DOF x_3. The frequencies are highlighted for the cases when the system is fully symmetric and fully asymmetric.

Table 3: Natural frequencies at the nominal value and limiting values of contact stiffness.

k_{s3} (N/m)	ω_1 (Hz)	ω_2 (Hz)	ω_3 (Hz)
$8.03 * 10^{-1}$	0.2	22.0	699.8
$8.03 * 10^{3}$	18.0	25.4	699.9

The formation of asymmetry results in a non-zero second component of the second mode shape. From Equation (5), this behavior leads to a resonance peak at the second natural frequency on all three DOFs, as seen in the linear forced response curves in Fig. 6. The six plots denote the frequency response of all three DOFs near each resonance due to a $25\ N$ force applied to only DOF, x_2. The first resonance peak decreases in frequency and amplitude towards 0 Hz as $k_{s3} \to 0$. The formation of the second resonance, with a nearly constant frequency and asymmetry-dependent amplitude, is also evident. Additionally, the third resonance is negligibly influenced by the asymmetry in terms of both frequency and amplitude.

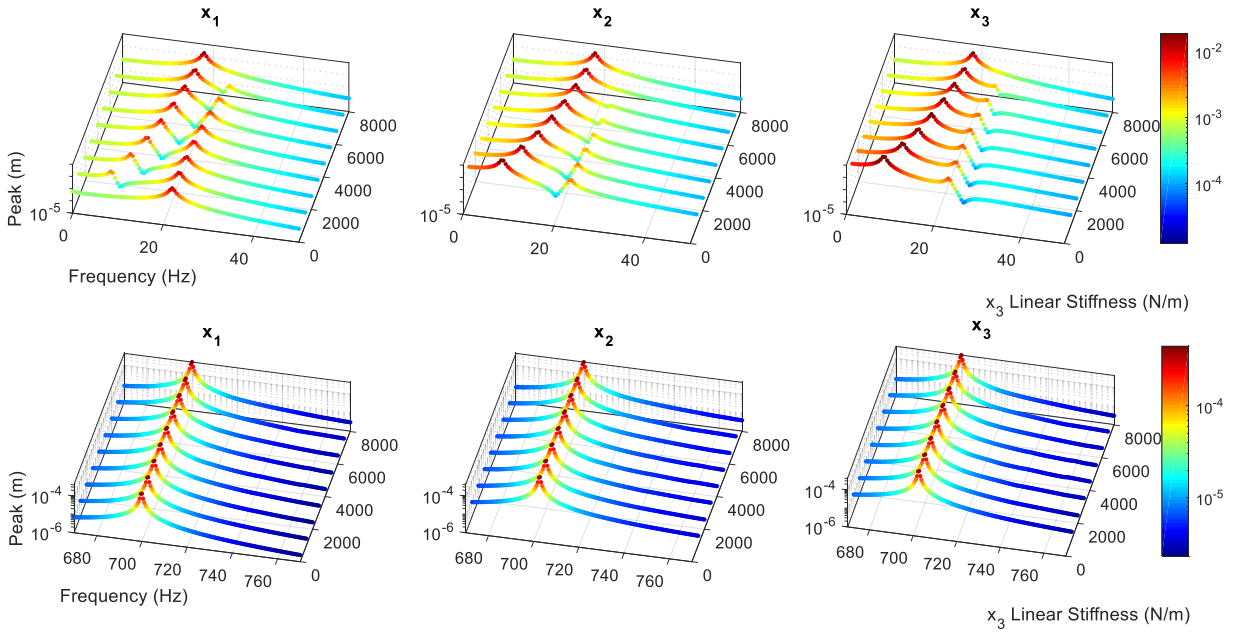

Fig. 6: 3D frequency response diagrams of all three DOFs with respect to forcing frequency and the linear stiffness on DOF x_3, for the purely linear system configuration. A forced excitation of $25\ N$ is applied to only DOF x_2. The colorbar denotes peak response amplitude.

The above results demonstrate how the primary factor behind the presence of the second resonance in the forced response curves is inherently due to the symmetry of the system. The location of the forced excitation is a secondary factor, as highlighted by Fig. 7. These plots denote the frequency response for all three DOFs as a function of the linear stiffness on DOF x_3, near each resonance. The forcing is modified to act with $25\ N$ on only DOF x_1. When the system is perfectly symmetric, the second resonance does not appear for the second DOF regardless of the forcing behavior on the system. Instead, only the first and third resonances exist. The forcing behavior governs the existence of the second resonance on the first and third DOFs, as the plots indicate the modified forcing induces the second resonance on DOFs x_1 and x_3. As the system loses symmetry, all three resonances again exist for the modified forcing and behave similarly to the default forcing configuration. The first resonance gradually disappears to 0 Hz on all DOFs as the asymmetry increases, the second resonance grows in amplitude on all DOFs, and the third resonance remains unchanged on all DOFs.

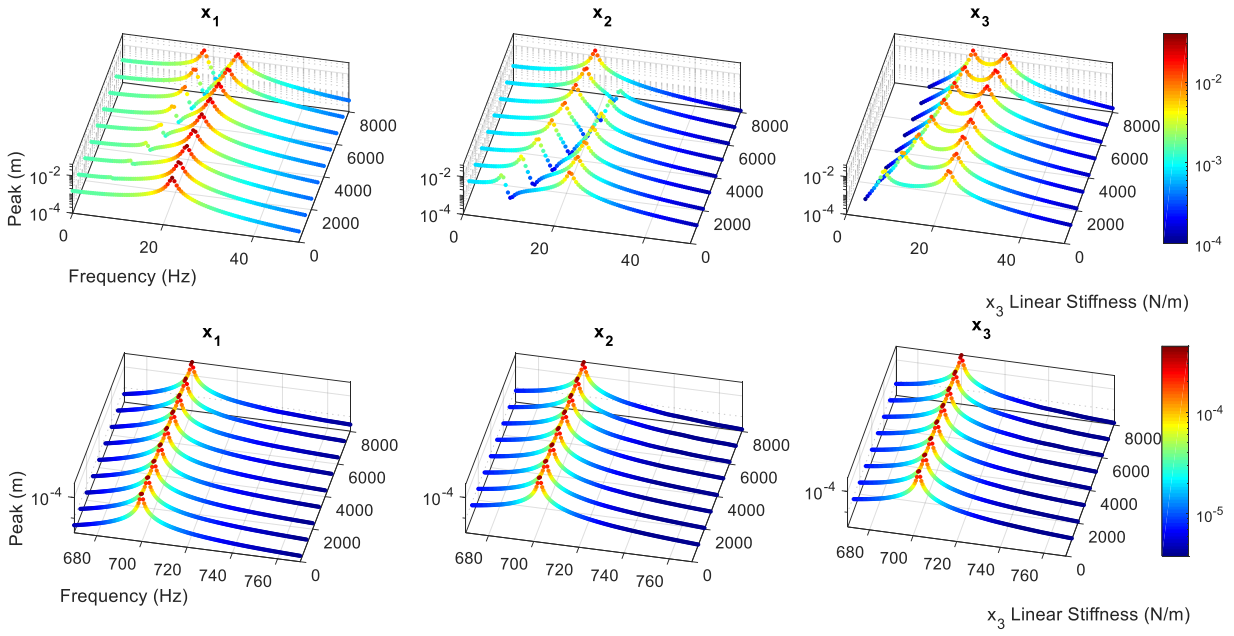

Fig. 7: 3D frequency response diagrams of all three DOFs with respect to forcing frequency and the linear stiffness on DOF x_3, for the purely linear system configuration. A forced excitation of 25 N is applied to only DOF x_1. The colorbar denotes peak response amplitude.

These results provide a baseline understanding of the linear dynamics of the system at the extreme limits of the operation, either at low or high levels of excitation. The observance of the peaks is understood well through the concepts of controllability and observability from linear system theory and modal analysis. The following sections demonstrate the behavior of the shaft-bearing system when operating in the nonlinear regime and how the nonlinearity introduces behavior that challenges the understanding of the dynamics based on linear theory. The results will also serve as a linear-system reference for the asymmetry study provided in Section 8.

4. Forcing excitation effects on the vibro-impact properties of the system

The nonlinear forced response curves are calculated for the nonlinear system using the two methods outlined in Section 2. The forcing is applied to the center of the impact beam (i.e., DOF x_2) with the nominal values given in Table 1, i.e. the symmetric system. Fig. 8 shows the frequency response curves for each DOF with respect to forcing magnitude p_2. The dash-dot line denotes the upper contact boundary, and it is evident that nonlinear behavior occurs only around the resonance peaks. Each curve is the combined result of multiple random ICs, and no isolas are detected away from the resonance peaks. The nonlinear behavior consists primarily of amplitude flattening due to the hard contact and significant frequency hardening of both the low- and high-frequency resonances. In addition, solutions are observed at both higher and lower frequencies than the resonance peak near 700 Hz.

The zoomed insets reveal a decrease in the stability of the solutions along the higher-amplitude branches due to the scatter of points at these excitation frequencies. Upon closer inspection, the entirety of each upper solution branch is found to be chaotic (see Fig. 9), and the system response jumps at an arbitrary time from the higher-amplitude chaotic attractor to the lower-amplitude periodic attractor. This jumping behavior causes the regions of 'scattered' solution points between 50-150 Hz and 650-750 Hz, and further simulations indicate this is due to the chaotic nature of the system at these frequency ranges. These regions are referred to as grazing-induced chaotic solution branches, since grazing behavior due to the contact springs causes the system response to become chaotic. Even small discretization errors from the time integration method are influencing the trajectory of the system, namely, by causing it to perturb and settle onto the lower-amplitude solution branch. The chaotic behavior is robust and is not just a numerical artefact; the small error persists both with and without the event location feature and with different ODE solvers (e.g., ode23, ode113, ode15s). This behavior was only observed for the case of chaotic solutions with hard contact stiffness values defined for k_g.

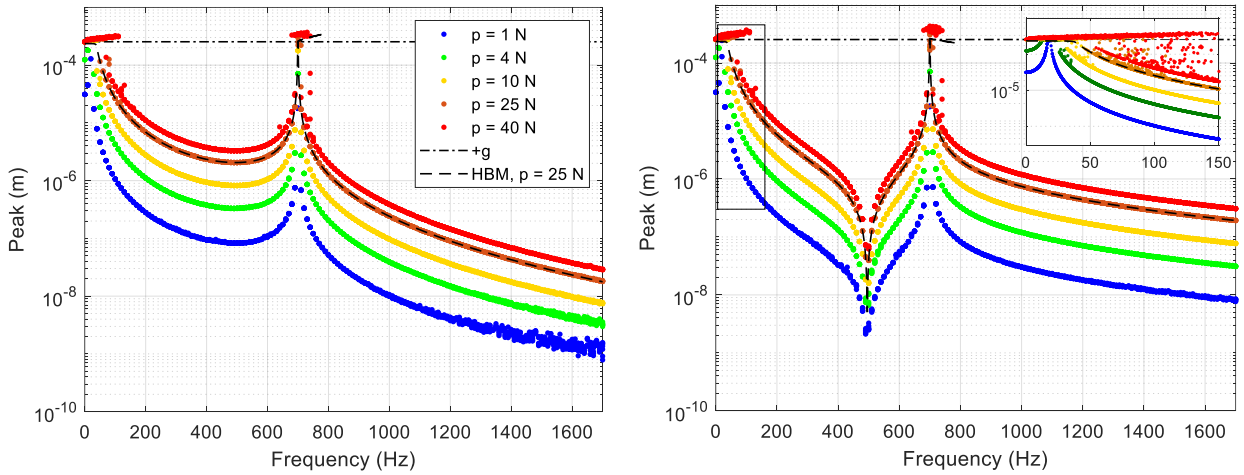

(a) x_1 (b) x_2

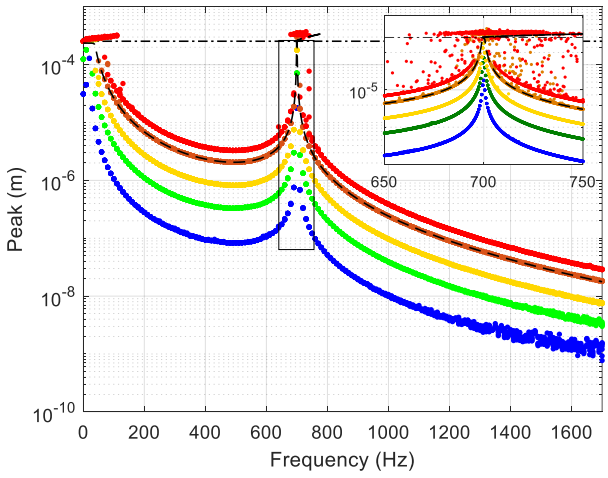

(c) x_3

Fig. 8: Frequency response curves for each DOF with respect to forcing magnitude p_2 applied at DOF x_2. The dash-dot line denotes the upper contact boundary, and the dashed line denotes the multi-harmonic balance response of the system when $p_2 = 25N$.

The system response for $p_2 = 25N$ is also obtained using the MHB solver with 36 harmonics, denoted with a black dashed curve in Fig. 8. The MHB results show excellent agreement with the lower solution branch, but some discrepancies exist near the resonance peaks. It captures a flat-top response of nearly constant amplitude from 0 Hz to about 38.2 Hz, with no presence of a turning point bifurcation. The MHB solution captures the hardening behavior of the third resonance peak near 700 Hz, with a region of multiple solutions. It is well-known that the MHB code can only capture periodic solutions, and so Fig. 9 further interrogates the solutions obtained from the numerical time integration for the steady-state responses of DOF x_1 at 25 Hz, 80 Hz, and 700 Hz. The plots are presented in terms of time histories, phase portraits, and Poincaré maps. It is evident that all three high-amplitude time-integrated responses are chaotic, as the Poincaré maps are irregular shapes and neither finite sets of points nor closed loops [29]. This confirms that the upper branches of solutions are unobtainable with the MHB solver in the case of hard contact. In addition, the responses at 80 Hz and 700 Hz are jumping from high-amplitude to low-amplitude solutions. As this behavior can occur at any arbitrary time due to the chaotic nature of the system, this behavior is unpredictable and is the source of the scatter of points between the upper and lower solution branches. At 80 Hz, the phase portrait and Poincaré map of both the high-amplitude chaotic response (blue with red dots) and the low-amplitude periodic response (yellow with black dots) are shown to highlight the change in behavior before and after the jump.

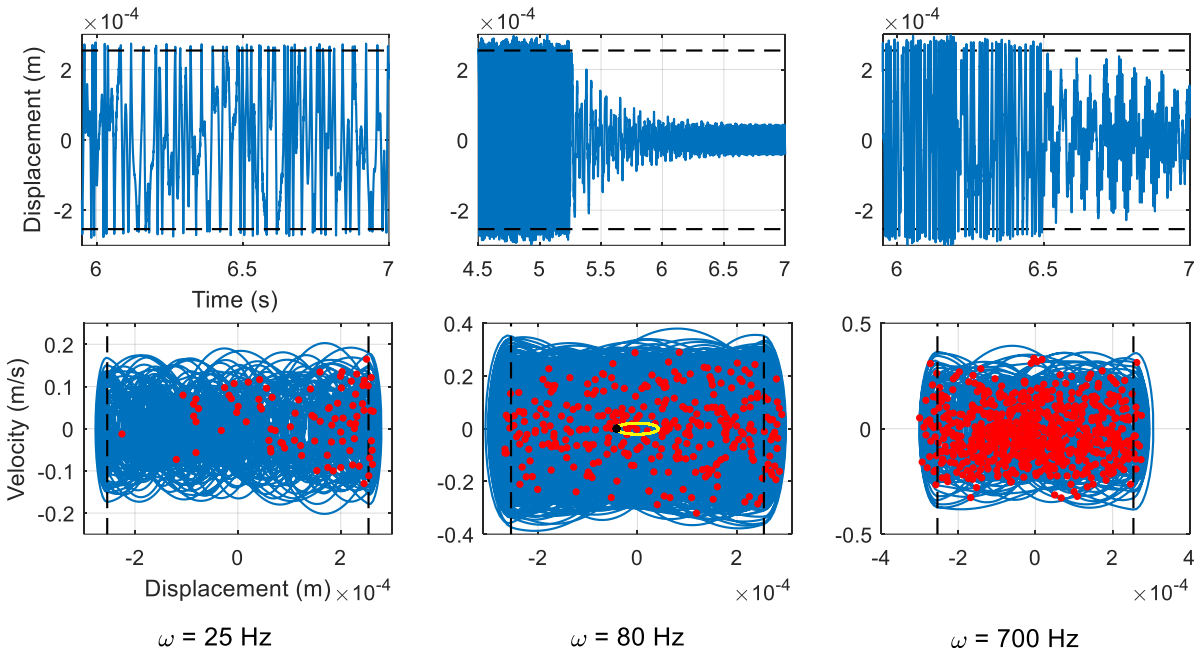

Fig. 9: Time history, phase portrait, and Poincaré map (dots) of DOF x_1 at three different forcing frequencies, and forcing magnitude 25 N, from Fig. 8. At 80 Hz, the phase portrait and Poincaré map of both the steady-state chaotic and steady-state periodic responses are shown using blue/red and yellow/black colors, respectively.

The presence of hard contact in the system presents challenges when predicting the nonlinear forced response. Discrepancies exist between the numerical time integrated solution and the MHB solver due to the chaotic nature of the system and the extreme sensitivity to initial conditions. These results highlight the need for careful interpretation of the results if only one solution method is utilized, and that chaos may go undetected if one solely relies on MHB.

5. Influence of the gap size on the system's response

As discussed previously, the experimental apparatus in [30] allows for several parameters to be altered to investigate the nonlinear dynamics of a shaft-bearing system with idealized clearances due to bearings. In this section, the focus is on the change of the gap size as these are readily adjusted by altering the spacing between the impact tips and impact beam with the rotation of a threaded rod. Fig. 10 shows the frequency response plots with respect to gap size around the two resonance regions, plotted in 3D for a clearer view, with a 25 N force applied at the middle DOF. The value range is chosen such that the largest gap size produces no contact even at the highest-amplitude resonance, resulting in limiting behavior of the system. The low-frequency resonance becomes flattened and shifted to higher frequency as the gap size decreases. Grazing-induced chaotic solution branches are again observed to occur over a widening frequency range as well, as observed by the presence of the scattered points. The resonance peak near 700 Hz is also flattened in amplitude as the gap size

decreases, but interestingly it expands to both lower and higher frequencies. However, there is no other formation of nonlinear behavior observed, such as isolas or superharmonic resonances, that can be explored in further detail.

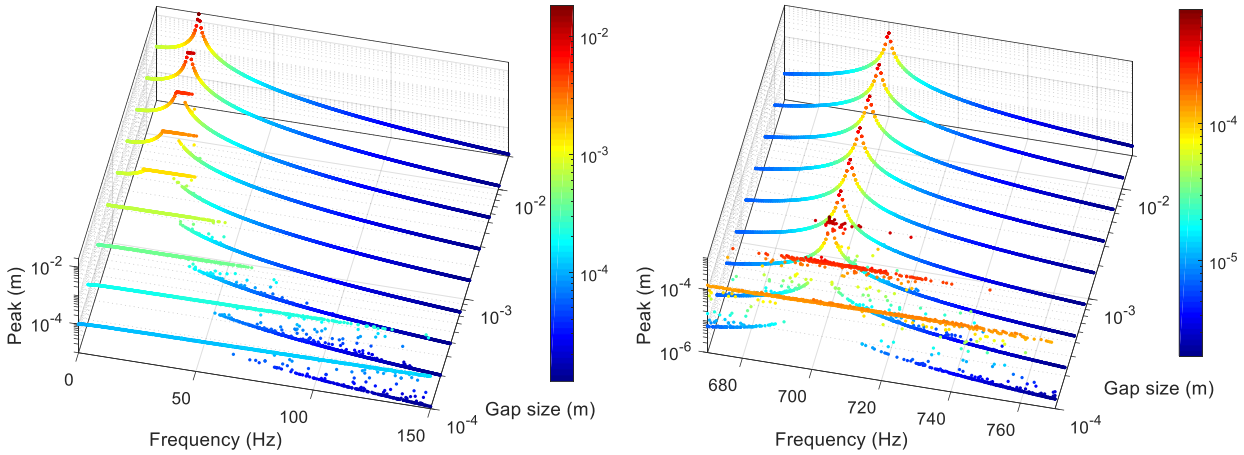

(a) $x_1, 0-150Hz$ (b) $x_1, 670-770Hz$

Fig. 10: 3D frequency response diagrams of DOF x_1 with respect to forcing frequency and gap size g. The colorbar denotes peak response amplitude.

The adjustment of the gap size in the contacts produces linear behavior in the extreme upper limit of gap size, as expected. As the gap size decreases, the solutions produce more grazing-induced chaotic responses and cause flattening of the resonance peaks, as was seen when varying the forcing amplitude. The onset of chaos can thus be realized with both changes of gap size and forcing amplitude, so long as the system has hard contact stops. The next section explores the evolution of behavior as the contact stiffness is changed.

6. Nonlinear characteristics of the shaft-bearing assembly due to contact stiffness

Next, the influence of the contact stiffness k_g on the shaft-bearing assembly is examined. This can be modified in the experimental apparatus by exchanging different hammer tips to adjust the stiffness of the contact occurring on the impact bar. The nonlinear behavior observed in the previous sections consisted primarily of chaotic behavior, which is likely due to the hard contact in the system. The system response is expected to show less broadband chaos when the contact stiffness becomes softer. This change is confirmed in Fig. 11, which presents the frequency response of DOF x_1 as a function of k_g for a 25 N force applied at the middle DOF. The corresponding plots for DOFs x_2 and x_3 are omitted because they appear nearly identical at both the low- and high-frequency resonances. The value range is chosen such that the softest contact stiffness has negligible effect on the system response, and the hardest contact stiffness (corresponding to the value in Table 1) induces a predominantly chaotic response region at low frequency.

The most notable feature in Fig. 11(a) as the hard contact stiffness is relaxed is the gradual formation of a resonance peak out of the region of chaotic solutions. This resonance decreases in frequency and grows in amplitude before settling near 20 Hz at soft stiffness. At frequencies higher than the resonance, there exist multiple bands of isolas that shift to lower frequency before disappearing for soft stiffness as well. At frequencies lower than the resonance, bands of nonlinear behavior are resolved out of the chaotic motions for hard contact stiffnesses. These bands experience slight frequency softening and become more distinct as the contact stiffness softens. Fig. 11(b) shows the system's response near the 700-Hz resonance, and the contact stiffness is significantly less influential at these higher frequencies. The resonance peak is high enough in amplitude to be subject to contact at all stiffness levels, but its frequency and amplitude is nearly unchanged until $k_g \approx 10^5 N/m$. As the hard stiffness is relaxed, the resonance resolves out of the region of chaotic motions, shifts slightly to lower frequency, and becomes a distinct peak. There exist two narrow ranges of contact stiffness near $k_g = 10^6 N/m$ at which solution points exist with higher amplitudes than the resonance peak.

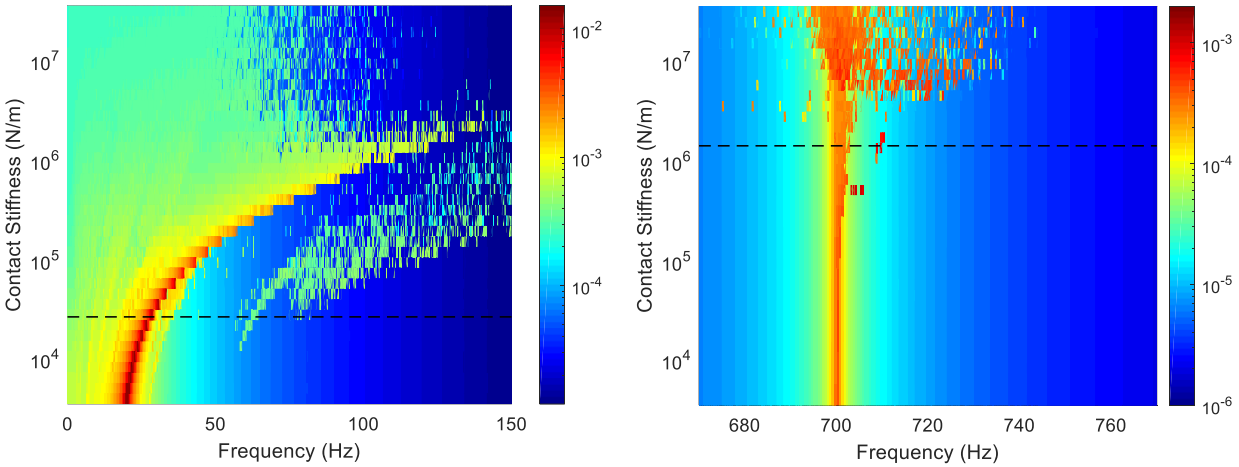

(a) $x_1, 0 - 150Hz$ (b) $x_1, 670 - 770Hz$

Fig. 11: Detailed frequency response diagrams of DOF x_1 with respect to forcing frequency and contact stiffness k_g. The colorbar denotes peak response amplitude. The dashed lines denote contact stiffnesses which are further studied in Figures 11 and 12.

Two intermediate values of contact stiffness are investigated in more detail, namely, $k_g = 2.626 * 10^4 N/m$ and $1.4 * 10^6 N/m$, which are indicated by the black dashed lines in Figures 10(a) and 10(b), respectively. The system response for the first frequency range (0 to 100 Hz) and contact stiffness ($k_g = 2.626 * 10^4 N/m$) pair is presented in Fig. 12 showing both the time integration and harmonic balance simulations. The overlay of the two approaches generally shows excellent agreement, except for a few regions. It is noted that the largest resonance peak is at 28.9 Hz, and there exist two subharmonic isolas of order 2 and 3 over the frequency ranges between 42-47 Hz and 55-73 Hz,

respectively. There are another two isolas over the frequency ranges 20-22 Hz and 74-85 Hz, consisting of quasiperiodic solutions, and there is another quasiperiodic region connected to the main branch from 32 to 35Hz. These solutions are only captured with the time integration method since the MHB solver is unable to capture non-periodic solutions.

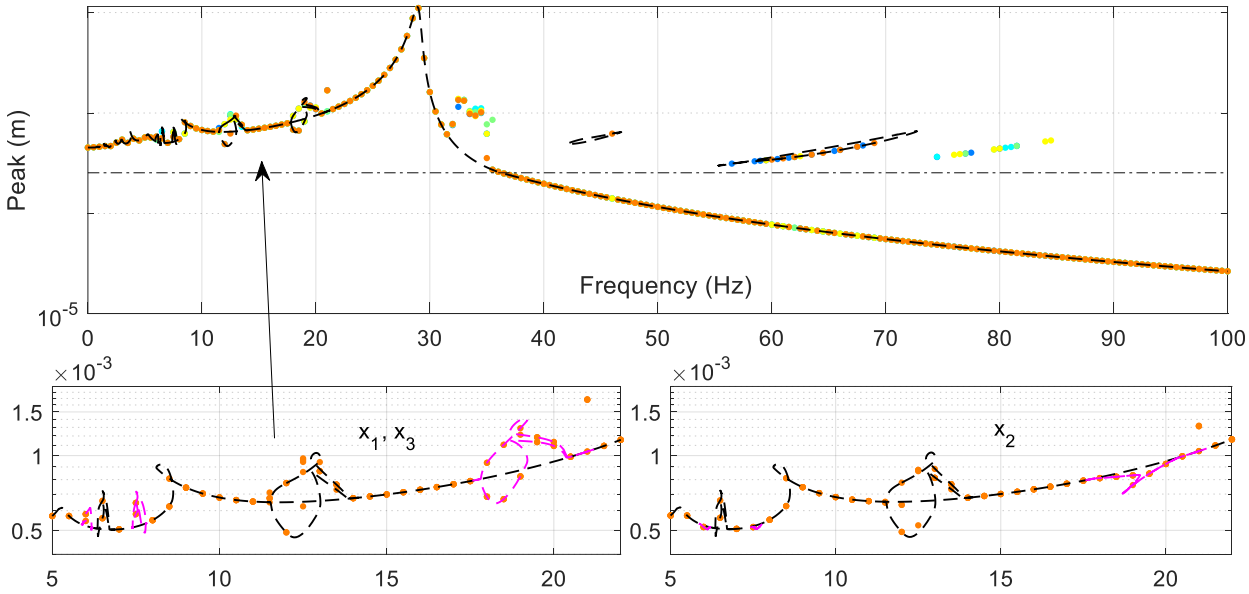

Fig. 12: Frequency response curve of the system in Fig. 11(a) for DOF x_1, with the contact stiffness fixed at $2.626 * 10^4 N/m$. The colored dots indicate solutions from the time integration solver. The dashed lines denote solution curves with the MHB solver. The dash-dot line denotes the upper contact boundary. In the smaller zoomed figures are the low-frequency response comparing DOFs x_1 and x_3 to DOF x_2; all time integration results are colored orange for clarity, and the pink curves denote superharmonic resonance branches of the second natural frequency.

At lower frequencies, below 21 Hz, numerous superharmonic resonances exist for this system configuration. The MHB solution shows that the shape of the resonance peak takes on two forms: the first relates to regions where the main solution branch loops around on itself, generating a "tongue" along the main branch. The other type of solution is where there exist separate solution branches that intersect the main branch tangentially and connect to the main solution branch at symmetry-breaking bifurcations [29]. In these regions, the upper and lower solutions at a given frequency are asymmetric pairs of coexisting solutions, meaning the time histories of each DOF on these branches tend to take the form $x_{upper}(t) = -x_{lower}(t)$, with a possible phase shift.

The time history behavior simulated with the MHB solver is shown in Fig. 13 for the two superharmonic resonances centered near 12 Hz and 18 Hz. It is observed that the symmetry-breaking behavior along the nonlinear forced response curve does not necessarily affect DOF x_2 on some of these superharmonic resonance branches. For example, near 12 Hz all three DOFs exhibit two pairs of asymmetric motions along the superharmonic resonance. For both motions, each DOF moves in unison

and thus the net behavior of the full system is a translational motion, resembling the behavior of the system's first linear mode. Near 18 Hz, however, only DOFs x_1 and x_3 exhibit two pairs of asymmetric motions, while both solutions for DOF x_2 are identical and symmetric in time about the rest position. This symmetry on DOF x_2 causes the full system to move with a rotational motion, resembling the behavior of the system's second linear mode. This is notable because the solution of all DOFs is expected to be symmetric in time based on the linear mode shapes and forcing at DOF x_2, but the contact nonlinearity introduces asymmetry into the system. Consequently, even though no primary resonance exists for the second natural frequency, the contact nonlinearity introduces superharmonic resonances of the second natural frequency. The superharmonic resonance branches with symmetric DOF x_2, i.e. which occur near 18 Hz, 8 Hz, and 6 Hz, make approximate integer ratios of $2:1, 4:1$, and $6:1$ with the second resonance frequency, which can be seen later in Fig. 21 is near 36 Hz. These resonance branches are colored pink in the zoomed plots of Fig. 12 to distinguish them from the superharmonic resonances of the first natural frequency, which experience total symmetry breaking due to the contact nonlinearity. This provides further evidence that the contact nonlinearity is activating the hidden second resonance that is not present from a linear analysis perspective.

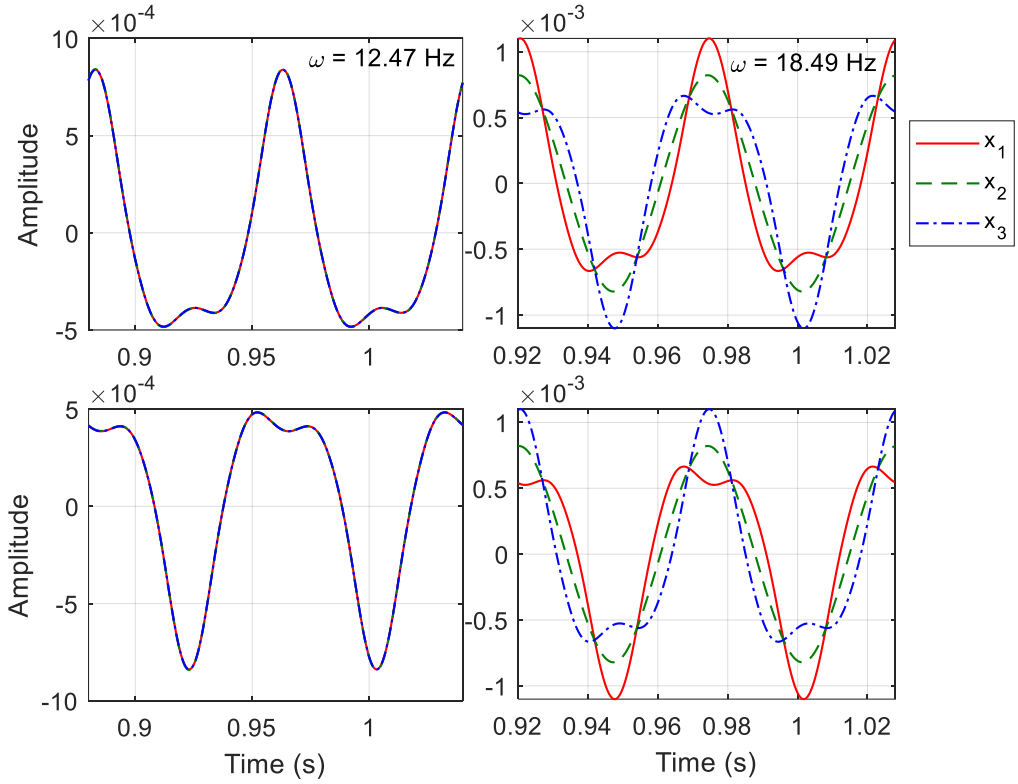

Fig. 13: MHB time histories of the system response on the superharmonic resonance solution branches highlighted in Fig. 12. Upper and lower plots correspond to solutions on the upper and lower solution branches, respectively. These solutions are captured near 12.47 Hz and 18.49 Hz.

Fig. 14 depicts the system response for the second frequency range and contact stiffness pair of interest, which was taken from the black dashed line in Fig. 11(b). Based on the MHB solution, the third resonance peak is observed to bend towards higher frequencies and produce a turning point bifurcation around 707 Hz due to hardening effect of the contacts. This produces a frequency shift of about 1%. In addition to the main resonance curve, several isolas exist around the primary resonance that are detached from the main solution, producing a cloud of isolas with frequencies below and above the main resonance peak. Given a forcing frequency ω and corresponding period T, these isolas correspond to period-n motions for which the solution's frequency is $\frac{\omega}{n}$ and period is nT. There are observed $n = 5,7,9,10,11,12,$ and 13. In addition, the highest-amplitude points seen between 710 and 715 Hz are parts of two quasiperiodic isolas that were only computed using numerical time integration. The family of isolas that exist around the third resonance peak explain the existence of solutions at frequencies below the linearized natural frequency, as the isolas span a broad bandwidth around the peak. These isolas are captured by using a single vector of Fourier coefficients as a starting guess and simply changing the order of the subharmonic in the MHB code. Further, isolas of each period-number appear in symmetry-complementing pairs. For example, there are two isolas of period $n = 7$ past the resonance peak, one for which x_1 has a larger amplitude than x_3 and one for which the opposite is true. This occurs because the system is inherently symmetric, so there is no difference between numbering the system DOFs relative to the left or right DOF. The individual DOF motions at a given frequency tend to be asymmetric, however, since the total system motion is primarily a combination of bending and rotation about DOF x_2.

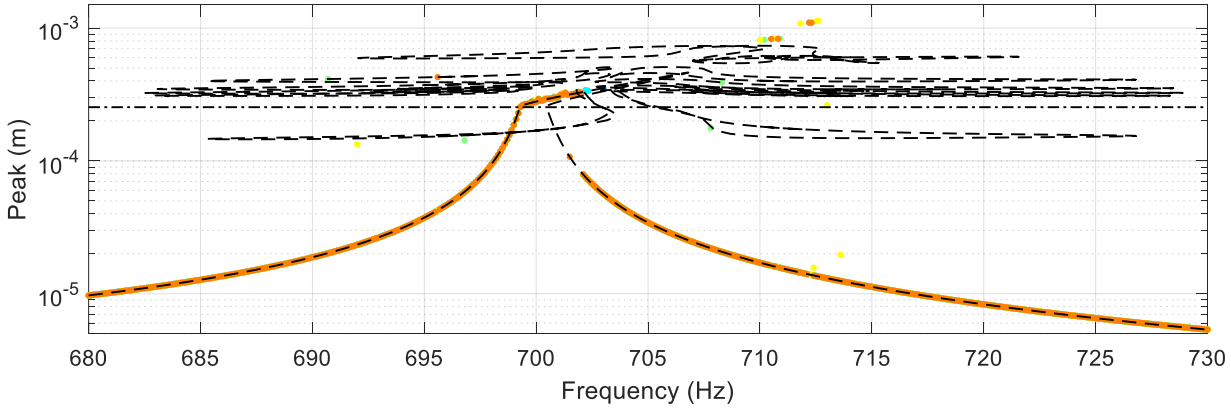

Fig. 14: Frequency response curve of the system in Fig. 11(b) for DOF x_1, with the contact stiffness fixed at $1.4 * 10^6 N/m$. The colored dots indicate solutions from the time integration solver. The dashed lines denote solution curves traced out with the MHB solver. The dash-dot line denotes the upper contact boundary.

A stability analysis is useful to determine to what extent these isolas can be realized in the experimental setup. Fig. 15 shows the stability of each MHB solution branch in Fig. 14. The time integration solutions are all colored blue for clarity, and the black and red dots correspond to stable and unstable MHB solutions, respectively. The majority of each isola is observed to be unstable, partially accounting for the sparsity of isolas captured with the direct time integration method. The distribution range from which initial conditions are randomly selected is the second explanation for the time integration results. Namely, initial displacements are set to be chosen from within the contact gap range, and initial velocities from within an arbitrary range a few orders of magnitude larger, i.e., $\{x_0\}_{1,2,3} \in [-g, +g]\ m$ and $\{v_0\}_{1,2,3} \in [-0.5, +0.5]\ m/s$. The relatively limited ranges of initial conditions may lead the system to settle onto the low-amplitude solution branch more often than if the initial conditions came from a larger range beyond the contact gaps.

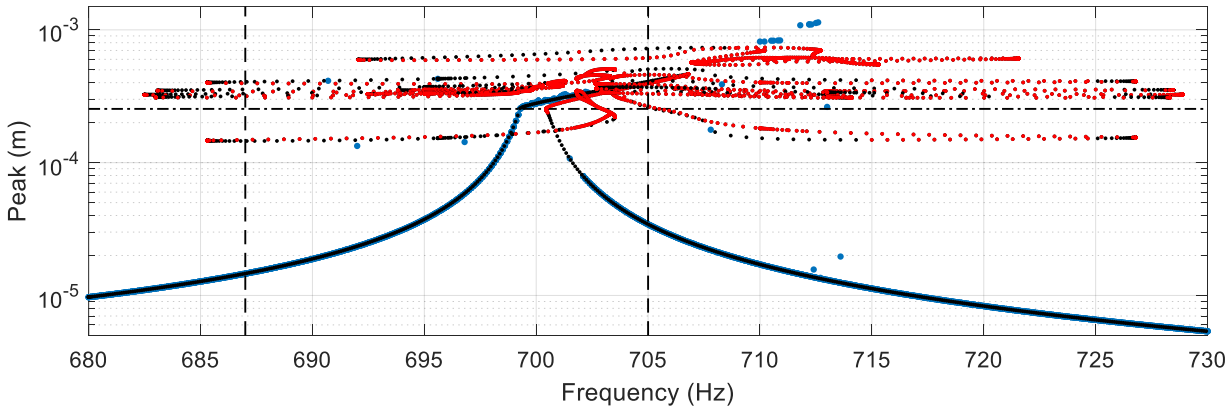

Fig. 15: Floquet stability results for Fig. 14 for DOF x_1. The blue dots denote time integration results, the black dots denote stable solution branches from MHB, and red dots denote unstable branches. The dash-dot line denotes the upper contact boundary. The vertical lines are placed at 687 Hz and 705 Hz, for which basins of attraction are later presented.

Given the family of isolas and their stability characteristics of the system's coexisting responses near the resonance in Fig. 15, the basins of attraction are computed using direct time integration to show the likelihood of the system settling onto any given attractor. Fig. 16 shows the basins of attraction at the two forcing frequencies of 687 Hz and 705 Hz. In both plots, the maximum values of DOF x_1 resulting from 10,000 sets of initial conditions are plotted against the corresponding initial displacement and velocity of x_1. The full range of initial conditions consists of 6-dimensional space, so a Latin Hypercube Sampling (LHS) scheme is utilized to efficiently obtain the total set of ICs used in the simulations. A larger range of initial displacements are employed for these simulations, i.e., $\{x_0\}_{1,2,3} \in [-10^{-3}, +10^{-3}]\ m$, to more easily capture the highest amplitude isolas seen in Fig. 15. The gap size is still the nominal value of $2.54 * 10^{-4} m$. Note that the white space in the plots represents

values where no sampling occurred. At 687 Hz, the difference between lowest- and highest-amplitude solutions is nearly a factor of 30, and six stable solutions are expected to coexist based on the result of the MHB solution. However, in Fig. 16(a) only three solutions are observed: the lowest-amplitude main branch solution, and two isolas. The basin for the lowest-amplitude solution takes up nearly the entire figure, to such extent that the only evidence for the isolas is two purple- and magenta-colored points near $(-5.3 * 10^{-4}\ m, -0.16\ m/s)$ and $(8.6 * 10^{-4}\ m, 0.72\ m/s)$.

Similarly, Fig. 16(b) indicates the main solution branch, post resonance, has the largest basin out of all solutions observed. This frequency (705 Hz) cuts through the main solution branch twice and through six isolas for a total of eight expected stable solutions, but only six of them are observed: the lower- and higher-amplitude main branch, isolas of period number $n = 5$ and 11, and two undetermined solutions. The amplitudes of the two undetermined solutions do not correspond to any of the frequency response results. They may be yet-undiscovered isolas with period-number greater than n $= 20$, or they may be quasiperiodic isolas. Regardless of the nature of the known and unknown solutions, there is still low likelihood that any arbitrary initial conditions or arbitrary perturbation will cause the system to settle onto any isola.

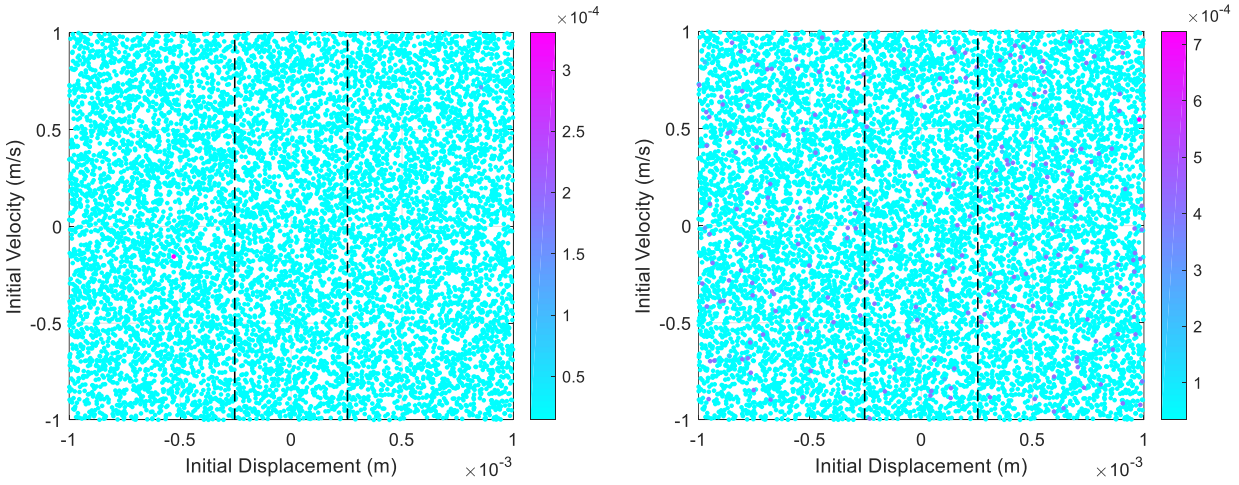

(a) $\omega = 687\ Hz$ (b) $\omega = 705\ Hz$

Fig. 16: Basins of attraction of the system in Fig. 14 at forcing frequencies of (a) $\omega = 687\ Hz$ and (b) $\omega = 705\ Hz$. In each figure, the color corresponds to the maximum value of $x_1(t)$, and the horizontal and vertical axes correspond to the initial conditions of x_1, i.e., $(x_1)_0, (v_1)_0$.

The adjustment of the contact stiffness produced a suite of complex nonlinear behavior for different stiffness values, ranging from hard to soft contact limits. A few interesting phenomena were specifically identified and interrogated, the first being the existence of superharmonic resonances of the hidden second primary resonance of the system. Due to the symmetry in the model and the choice of excitation location, the second resonance does not get excited; however, it was discovered that the

superharmonic resonances appear at low frequencies in one of the investigated configurations. There exist symmetry-breaking bifurcations along the main solution branch at low frequencies that could be realized during experiments performed on the test apparatus. It was also discovered that a cloud of isolas exist in the vicinity of the third resonance peak, providing further explanation of the observed solutions at frequencies below and above the main resonance. Stability analysis and the computed basin of attraction reveal that these solutions are unlikely to be realized for these system parameters, but this may not necessarily hold generally true for other configurations.

7. Damping modeling effects on the system's response

This section explores the effect of the viscous damping model on the system's dynamics. The representation of the damping for the shaft-bearing assembly influences the nonlinear characteristics of the system, and it is often challenging to determine which form to utilize since damping mechanisms come from various sources. Since an accurate model of the damping is not known with certainty, two different models are chosen for study, namely, the model using discrete grounded dashpots attached to each mass as proposed by Goldberg et al. [30], and a more conventional type based on mass proportional damping. Both damping models are as follows:

$$\mathbf{C}_1 = \begin{bmatrix} c & 0 & 0 \\ 0 & c & 0 \\ 0 & 0 & c \end{bmatrix}, \qquad \mathbf{C}_2 = \begin{bmatrix} c & 0 & 0 \\ 0 & 2c & 0 \\ 0 & 0 & c \end{bmatrix} = \frac{c}{m}\mathbf{M} \tag{5}$$

Fig. 17 shows the effects of the first damping model around the primary resonances as the damping coefficient is varied from the nominal value in Table 1 to 46 times the nominal value. All other parameters are held nominal to Table 1, and only the results for DOF x_1 is shown, since the results for all three DOFs look similar. The frequency responses are originally computed by varying the damping within an uncertainty range of $\pm 15\%$ of the nominal damping, but this proves to not influence the system response. Fig. 17(a) shows that the system's response at low frequency is moderately affected by an increase in damping. At all damping values, the upper solution branch from 0 Hz to 100 Hz is still abruptly limited in amplitude by the contact boundaries. The large cloud of points, which result from the system jumping from the higher solution branch to the lower branch, disappear with increased damping. The maximum frequency to which the upper branch extends is shortened from almost 100 Hz to about 27.5 Hz. Simultaneously, the hysteresis region between the lower and upper branches also shrinks and the branches nearly coalesce for the highest damping. There are no isolas observed for any damping values. However, there is a superharmonic resonance or other nonlinear behavior present for large damping below 25 Hz that is explored in more detail later in this section. At higher frequency, Fig. 17(b) depicts that the resonance peak with nominal damping is flattened and extends to both lower

and higher frequencies. This behavior quickly disappears as the damping increases, resulting in a much lower-amplitude resonance peak that falls within the contact gap and gradually widens out with increased damping. There is no indication of isola or any other nonlinear behavior around this resonance.

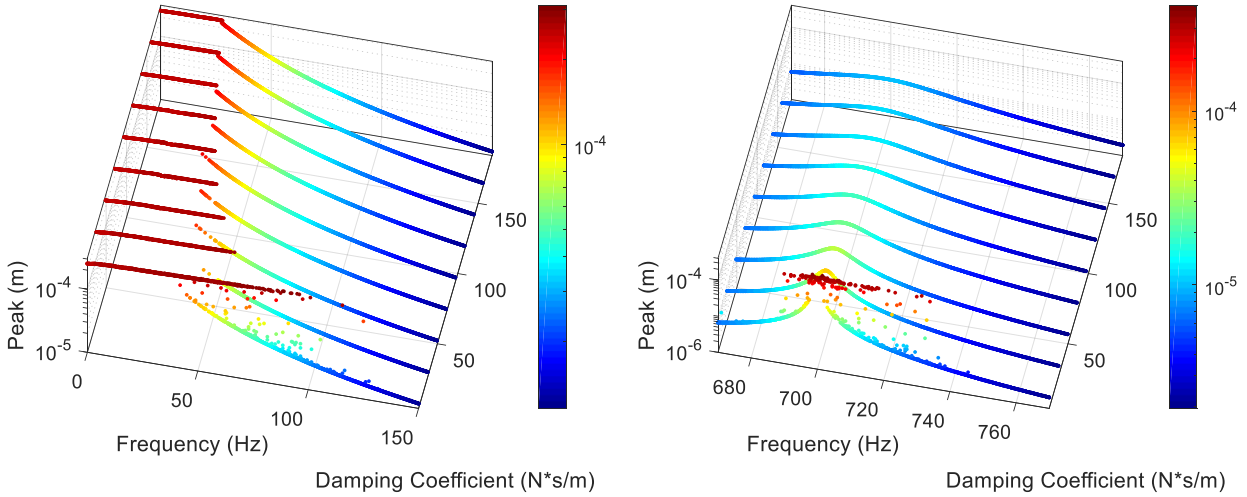

(a) $x_1, 0 - 150Hz$ (b) $x_1, 670 - 770Hz$

Fig. 17: 3D frequency response diagrams of DOF x_1 with respect to forcing frequency and damping coefficient c, using the damping model assumed by Goldberg et al. [30]. The colorbar denotes peak response amplitude.

The frequency response results of the second damping model are observed to be similar to the results of the first model and are omitted for brevity. The most notable difference is in the nonlinear behaviors observed at low frequency for large damping, which is explored in Fig. 18. The frequency response of the system with a damping coefficient of $139\ N*s/m$ is plotted using both the original and the proportional damping models, and distinct branches of high-amplitude solutions become visible for both models. The time histories of the various solutions at 5 Hz, 15 Hz, and 25 Hz are plotted underneath. At 5 Hz, one solution is present for both models, in which the system experiences chattering behavior (i.e., a cascade of contacts with increasingly rapid occurrence) as it comes into contact with either the upper or lower contacts [38, 39, 40]. The chatter occurs until the system comes out of contact altogether. The MHB procedure is unable to resolve this behavior because the chattering behavior itself is aperiodic in form. At 15 Hz, the solutions for the two damping models start to differ. The original damping model induces several similar types of solutions which differ mainly around the points of contact. These responses tend to come into contact with each contact boundary twice without chatter behavior. The proportional damping model, however, shows a single solution which still resembles chatter with two or three contacts occurring with each contact boundary. At 25 Hz, the original damping model induces two solutions which resemble chatter with only the lower contact

boundary, and one solution which hits each contact boundary once without any chatter. The proportional damping model induces two solutions, one with chatter and one without chatter.

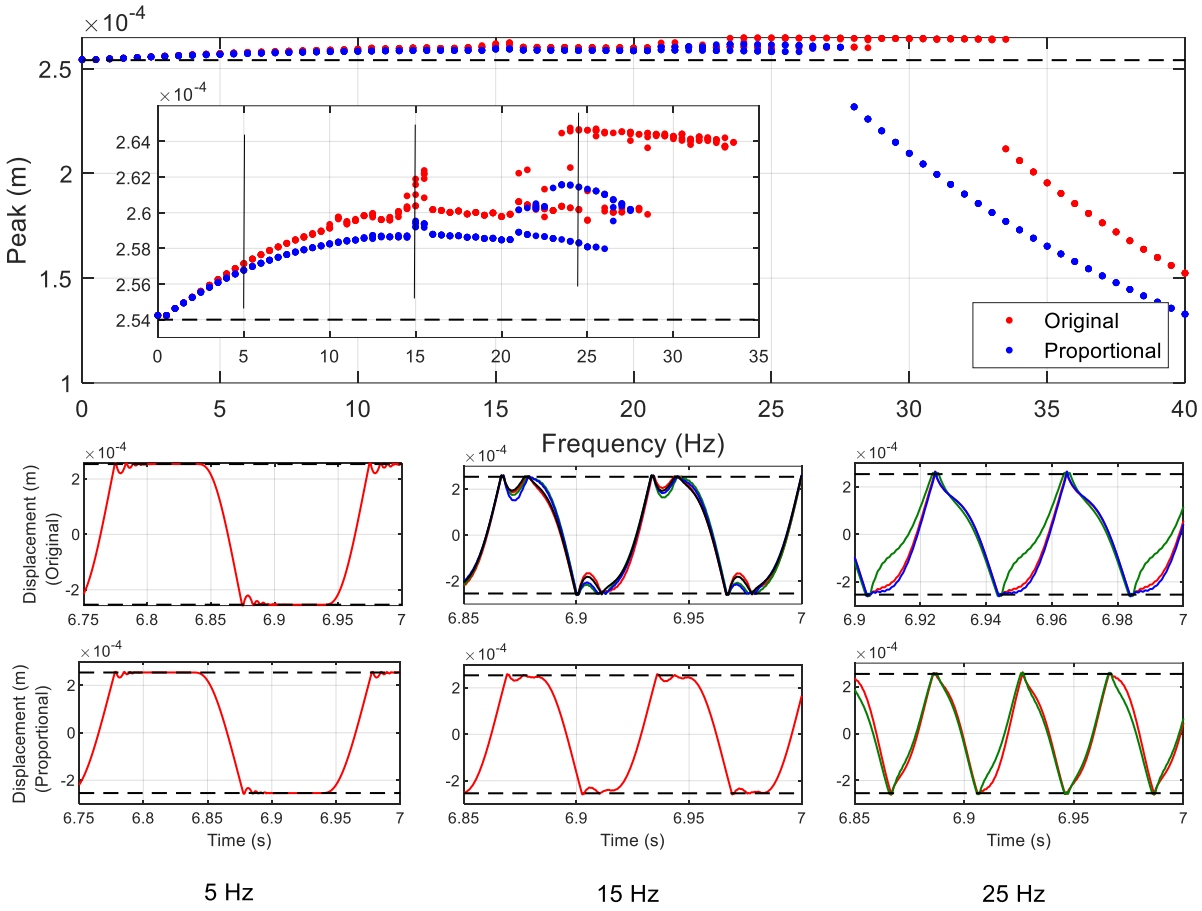

Fig. 18: Frequency responses and time histories of the system at 5, 15, and 25 Hz, with both the original and the proportional damping models with damping coefficient $c = 139\ N * s/m$. In the large plot, red and blue denote time integration results for the original and proportional damping models, respectively. In the small plots, the different colors denote the time histories of coexisting solutions at each frequency in no particular order.

Fig. 19 explores the chatter behavior by showing a zoomed in time history, phase portrait, and frequency spectrum of the system response at 5 Hz with the original damping model. It is clear from the phase portrait that the system response away from the contact events behaves periodically, but the response nearby the contact points behaves irregularly. The net result of these two behaviors is to make the overall response aperiodic. The Poincaré map is an irregular shape, implying chaos. The frequency spectrum shows there are harmonics of the forcing frequency up to 2,000 Hz, but there is not broadband frequency content between the harmonics that would further suggest the response is chaotic. The harmonic peaks tend to decay according to a $-3/2$ power law with frequency. There is also a decrease

in the harmonic content from 200-700 Hz. These results explain why the MHB solver is unable to capture this solution, even if up to 360 harmonics are used.

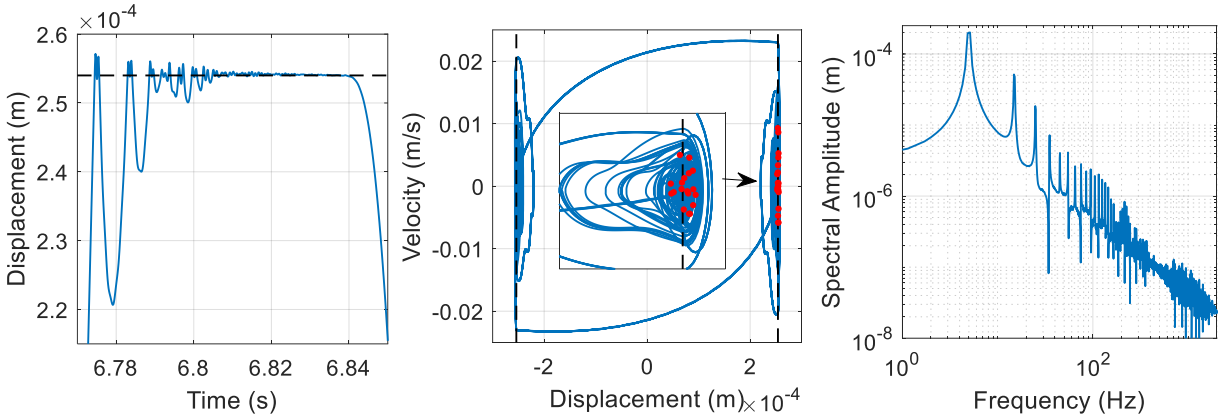

(a) (b) (c)

Fig. 19: (a) Time history, (b) phase portrait and Poincaré map (red dots), and (c) frequency spectrum of the system response at 5 Hz, with the original damping model and damping coefficient $c = 139\ N * s/m$. The dashed lines denote contact boundaries.

8. Existence of asymmetry and its effects on the system's nonlinear characteristics

The effects of the parameters that contribute to the inherent symmetry in the shaft-bearing assembly are explored at a high level to examine their influences on the dynamical responses of the system. These parameters are the linear stiffnesses, the contact stiffnesses, and the gap sizes on DOFs x_1 and x_3. In the next results, the system is made inherently asymmetric by keeping the value of each parameter on DOF x_1 constant and setting the parameter value on DOF x_3 to vary over a range of values. This is valuable because the actual physical apparatus is unlikely to be perfectly symmetric in its shape and in every parameter of interest. As in Section 7, each parameter is initially varied over an uncertainty range of $\pm 15\%$ to explore the effects of small and moderate asymmetries on the robustness of the system response. All three asymmetries have minimal influence on the system's response given this uncertainty range. This implies that the nonlinear system has a level of robustness against asymmetries in the physical system, and these original results are omitted for brevity. It is then desired to explore the limits of this robustness with much larger parameter uncertainties, and to observe trends in behavior that were seen in the previous sections.

Fig. 20 shows the frequency responses of DOF x_1 under the variation of the linear stiffness of DOF x_3, for both a soft and hard symmetric contact stiffness. Namely, the soft stiffness $2.626 * 10^4 N/m$ from Fig. 11(a) and the nominal hard stiffness from Table 1 are studied. The responses for the upper-most values of x_3 linear stiffness are symmetric and are thus equivalent to the results in Fig. 12 and Fig. 8 (orange curve), respectively. The results for DOFs x_2 and x_3 are similar and are omitted. The

system response in Fig. 20(a) and 20(b) differs from the linear case of Fig. 6 in that the second resonance forms near 40 Hz and grows in amplitude as the asymmetry appears. Further, the first resonance does not shrink to 0 Hz but decreases from 29 Hz to 24.5 Hz. Fig. 21 plots the natural frequencies as linear stiffness k_{s3} varies, analogous to Fig. 5, but with the contact gaps fully closed so the contact stiffnesses are added and the system configuration is linear. The first resonance is now easily seen to plateau, and the third resonance is observed to change negligibly. At lower frequencies, the same superharmonic resonances from Fig. 12 are present and do not vary significantly with the asymmetry. Isolas remain present between 40-100 Hz. One isola at the lower end of this frequency range grows with the asymmetry, while one at the higher end gradually disappears. Another isola appears to form and then disappear as asymmetry increases. The system's third resonance remains unchanged in both frequency and amplitude as the asymmetry changes. As in Fig. 12, there is no evidence of isolas around the third resonance peak for the soft value of contact stiffness.

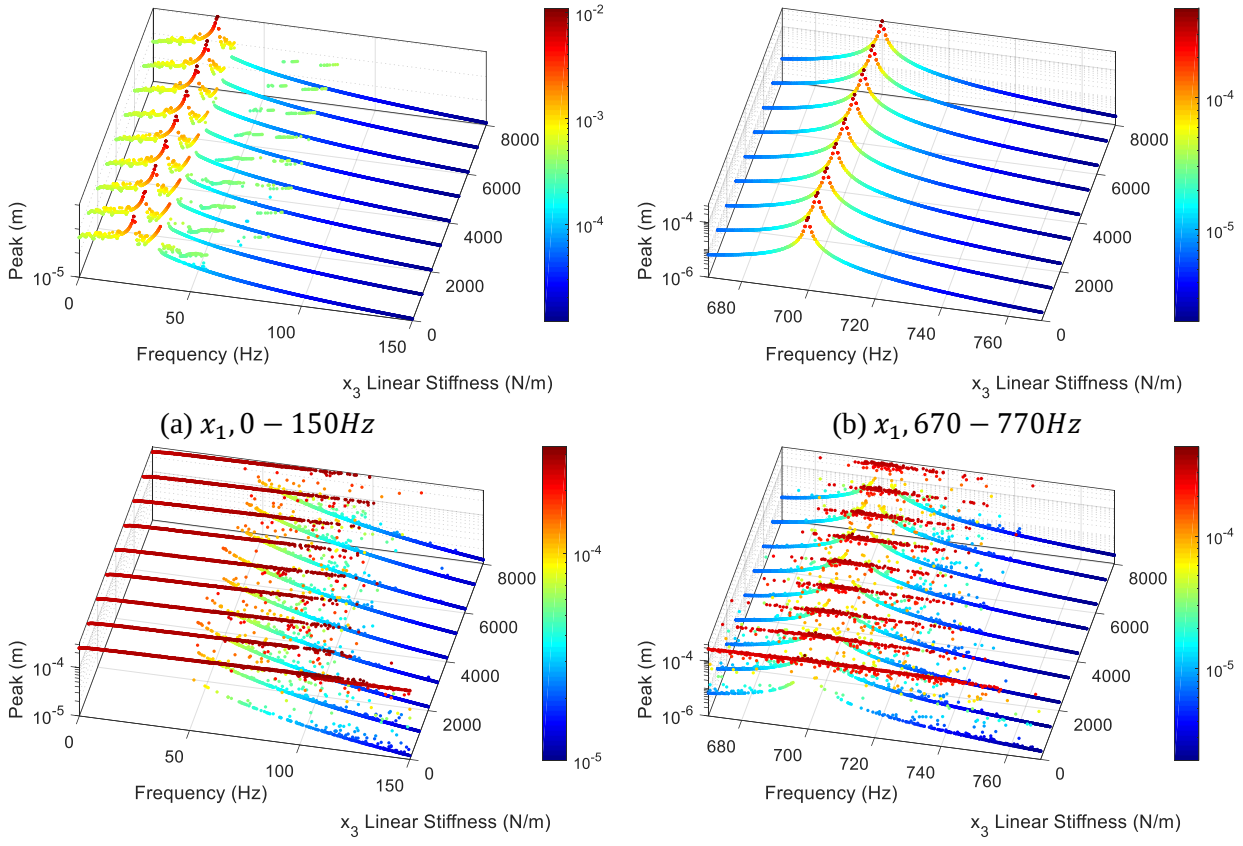

(a) $x_1, 0-150Hz$ (b) $x_1, 670-770Hz$

(c) $x_1, 0-150Hz$ (d) $x_1, 670-770Hz$

Fig. 20: 3D frequency response diagrams of DOF x_1 with respect to forcing frequency and the linear stiffness on DOF x_3, for both (a, b) soft and (c, d) hard contact stiffnesses. The colorbar denotes peak response amplitude.

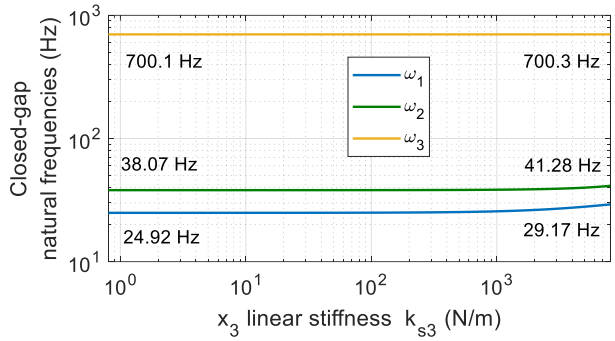

Fig. 21: Linear natural frequencies shapes as functions of the linear stiffness on DOF x_3, when the contact gap is fully closed $g = 0$ and contact stiffness is $k_g = 2.626 * 10^4 N/m$. The labels indicate the frequencies at the left and right ends of the plot where the linear stiffness is asymmetric and symmetric, respectively.

The system response with hard contact stiffness in Figures 19(c) and (d) is largely unaffected, both at low frequency and high frequency, as the linear stiffness of x_3 decreases to zero stiffness. In Fig. 20(c) at low frequency, the system exhibits the flattened upper solution branch of chaotic solutions and jumping behavior from upper branch to lower branch that was observed previously in Fig. 8. Both of these behaviors are present as the x_3 linear stiffness decreases to $0\ N/m$, and the only notable change is that the maximum frequency of the upper branch extends from 100 Hz to about 150 Hz. There is no other nonlinear behavior present, such as isolas or superharmonic resonances. In Fig. 20(d) at high frequencies, similar results are observed in the upper solution branch around the resonance peak. A moderately or significantly asymmetric linear stiffness on x_3 has little effect on the amplitude, frequency range, or jumping behavior of the upper branch, until the stiffness is zero. At zero linear stiffness, the frequency range of the upper branch extends from about 680-740 Hz to about 670-760 Hz. Otherwise, there are no other nonlinear behaviors, such as isolas, present around the resonance peak.

Fig. 22 shows the frequency responses of all three DOFs under the asymmetry variation of the contact gap size of DOF x_3, holding the contact parameters on DOF x_1 nominal from Table 1. It is clear that the system is significantly more sensitive to the x_3 gap size than to the x_3 linear stiffness, so these plots are created with more detail and are viewed from above for clarity. At low frequency in Fig. 22(a), as the gap size increases and becomes more asymmetric, a second resonance branch appears out of the original upper branch. This second upper branch grows in amplitude and shrinks in frequency range, and for the largest gap sizes it forms a resonance peak near 22 Hz. This solution branch is most easily seen in the x_2 or x_3 DOFs than in the x_1 DOF. The original upper branch of solutions remains relatively unchanged. There are no isolas observed at frequencies beyond 50 Hz, but there is faint

superharmonic resonance behavior present which forms below 20 Hz as the gap size increases. At high frequency in Fig. 22(b), the upper solution branch around the resonance peak is lower in amplitude than the resonances at low frequency, and it is less affected by the asymmetric gaps. The clouds of points jumping from high to low amplitude shrink in frequency range towards the resonance peak as the gap increases. The frequency and amplitude of the resonance peak itself does not change. For gap sizes larger than 10^{-3}m, there are several solid lines of intermediate amplitude (i.e., yellow and orange) which may indicate the presence of isolas around the resonance peak. This resembles the system's behavior as seen in Section 6 and is not studied further here.

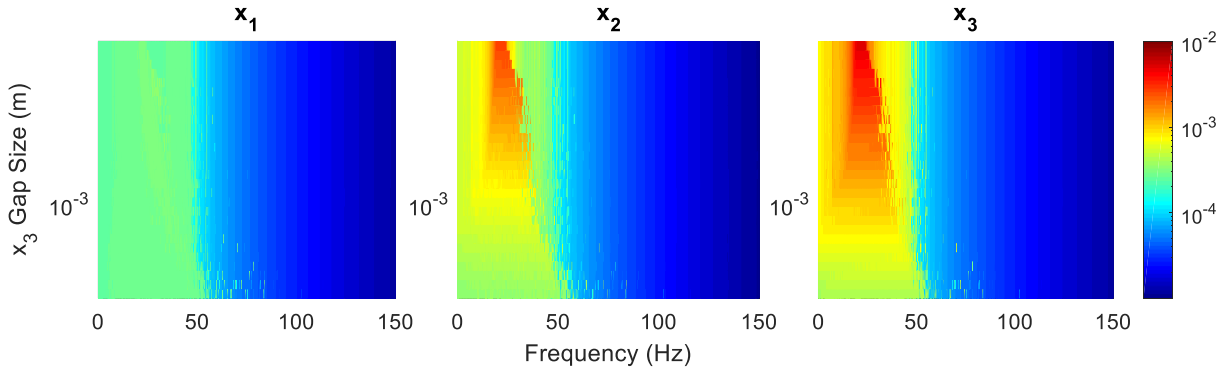

(a) $0 - 150Hz$

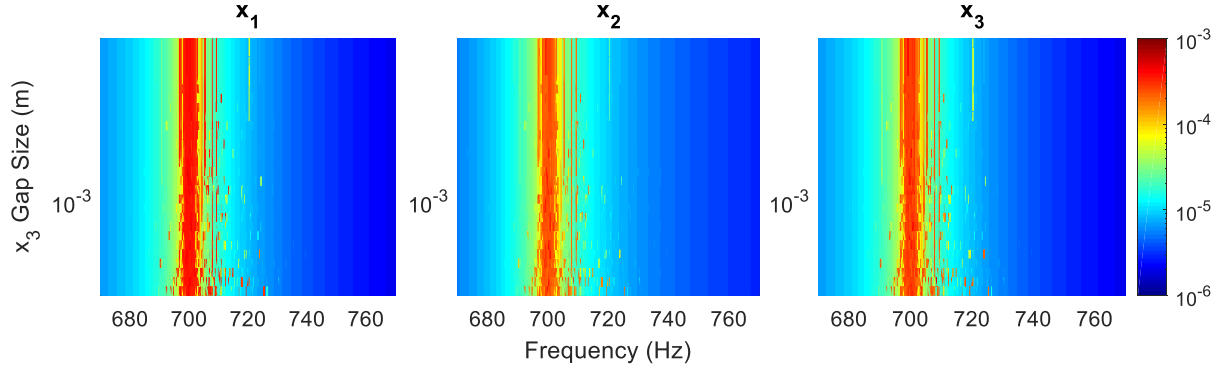

(b) $670 - 770Hz$

Fig. 22: Detailed frequency response diagrams of all three DOFs with respect to forcing frequency and the contact gap size on DOF x_3. The colorbar denotes peak response amplitude.

The last parameter of interest is studied in Fig. 23, which shows the frequency responses of all three DOFs under the variation of the contact stiffness size of DOF x_3. The contact parameters on DOF x_1 are nominal from Table 1. As with the x_3 gap size, the system response is significantly influenced by the contact stiffness. The system becomes more asymmetric as the stiffness decreases, and another high-amplitude resonance peak is again observed to form and converge towards 21 Hz. This resonance does not appear to form until the x_3 stiffness is below about $10^6 N/m$, at which point the resonance forms between 100-150 Hz and begins to both increase in amplitude and decrease in frequency towards

21 Hz. The original upper solution branch, extending from 0 Hz to between 50 and 100 Hz, still exists and remains relatively unchanged by the decreasing x_3 contact stiffness. The high-amplitude points above 100 Hz, near the formation of the resonance peak, may be isolas. These isolas form only for contact stiffnesses at least one to two orders of magnitude harder compared to the isolas seen in Section 6. The cloud of intermediate amplitudes (i.e., green color) near 50 Hz for contact stiffnesses less than about $10^5 N/m$, when plotted in 3D, are simply due to solutions jumping from high to low amplitude and do not indicate some other nonlinear behavior. At frequencies below the highest resonance peak, there exist small bands of additional nonlinear behavior, likely superharmonic resonances as seen in Section 6.

The high-frequency resonance is shown in Fig. 23(b), and it is more affected by the x_3 contact stiffness than by the x_3 gap size. A cloud of high-amplitude solutions is seen extending from about 680 Hz to 740 Hz for hard contact stiffness, and this frequency range decreases to about 695 Hz to 715 Hz as the contact stiffness softens. The resonance amplitude for DOF x_1 remains constant, but the resonance peaks for DOFs x_2 and x_3 noticeably decrease in amplitude as the contact softens below $10^6 N/m$. None of the high-amplitude solutions away from the resonance peak are characteristic of the isolas seen in Section 6; they simply indicate the point scattering behavior due to chaos.

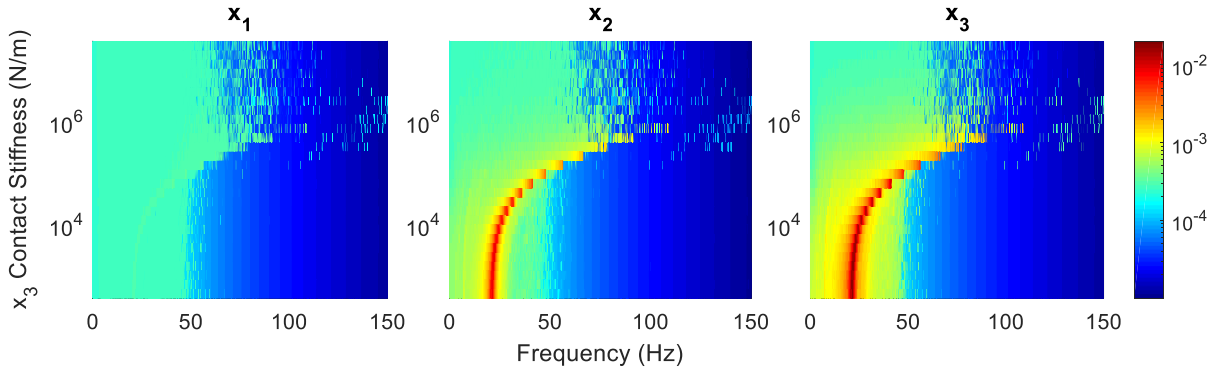

(a) $0 - 150Hz$

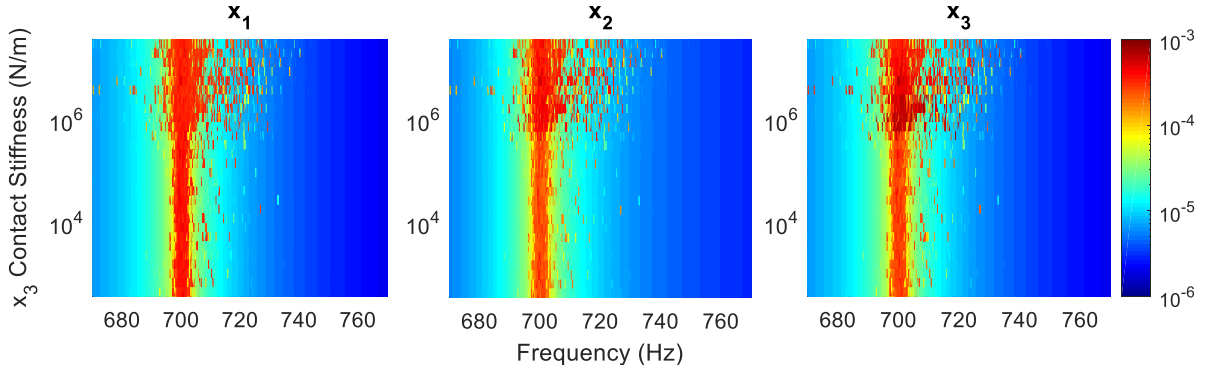

(b) $670 - 770Hz$

Fig. 23: Detailed frequency response diagrams of all three DOFs with respect to forcing frequency and the contact stiffness on DOF x_3. The colorbar denotes peak response amplitude.

9. Conclusions

In this work, the nonlinear frequency responses and characteristics of an idealized shaft-bearing assembly, operating as a vibro-impact system due to the bearing clearances, have been investigated. The system is versatile in that many design variables such as spring and contact stiffnesses, gap sizes, and forcing levels and locations can be easily changed to produce symmetric, asymmetric, linear, and nonlinear configurations. Several complex nonlinear dynamical behaviors were observed and characterized using both time integration and harmonic balance methods. Regions of chaotic solution branches were observed over a wide frequency range near each primary system resonance, and these became more evident with increasing levels of forcing or decreasing contact gap sizes. These regions of chaos are initialized by grazing bifurcations. The chaotic behavior can be mitigated by relaxing the system's nominally hard contact stiffnesses, and doing so also leads to the formation of isolas and secondary resonances over the frequency ranges of interest. Superharmonic resonances of both the first and second resonant frequencies were observed, even though there was no primary resonance peak for the second natural frequency due to the system's symmetry.

Branches of quasiperiodic isolas were also discovered after the first resonance. These can currently only be captured using the time integration, but there has been recent promising work combining harmonic balance and continuation principles for quasiperiodic motions [41, 42, 43]. Around the high-frequency third resonance, a cloud of many isolas formed. A basin of attraction analysis showed the system has low likelihood of settling onto any of these isolas if perturbed. Chaotic behavior in the nominal system can also be reduced by increasing the damping level. An additional result was the presence of chatter behavior at low frequency excitation, which could only be predicted with the time integration approach. The chatter was persistent and observed using both the original damping model proposed by Goldberg et al. [30] and a mass-proportional model.

The complex nonlinear behaviors described above were also evidenced in various asymmetric system configurations with unequal linear stiffnesses, gap sizes, or contact stiffnesses. Initial studies showed the system was insensitive to parameter asymmetries of as much as $\pm 15\%$, indicating the experimental setup is likely robust to small discrepancies in spring stiffnesses, gap sizes, etc. An asymmetry in the linear stiffness is less influential on the dynamics of the nonlinear system than on the dynamics of the linear system, both for harder and softer contact stiffnesses. It did, however, cause the first resonance to fundamentally change behavior: it plateaued to a constant natural frequency when the contact springs were present and fully closed rather than decrease to 0 Hz as it does without the

contact springs. Low frequency superharmonic resonances are unaffected, but different isolas can either grow or disappear as asymmetry grows. Two resonance peaks occur at low frequency if there is an asymmetry in either the gap sizes or the contact stiffness, and there was evidence of both isola formation and superharmonic resonances as well for specific design values. There was evidence of isola behavior around the high-frequency resonance, which was relatively unchanged from the symmetric configurations.

The results of this work can help to better understand the types of nonlinear behaviors that may occur in bearing-shaft systems. For example, ball bearings produce small gaps between the inner and outer races leading to intermittent contact behavior. The clearances and stiffness are functions of the bearing design, and thus the results from this research highlight the influence of these parameters on the performance of an idealized bearing-mounted shaft. Furthermore, the results of this study can be used to inform and design further experiments on the simplified physical system to study the various, complex phenomena predicted by the system model. Future work would benefit from further experimental validation of the system model. Namely, a more certain representation of the damping in the system, along with the influence of any contact damping, would be valuable.

Acknowledgements

B.E. Saunders acknowledges the help of Timothy Alvis of New Mexico State University for sharing the code for the Latin hypercube sampling scheme used in this work. B.E. Saunders and A. Abdelkefi gratefully acknowledge the support from Sandia National Laboratories. This study describes objective technical results and analysis. Any subjective views or opinions that might be expressed in the paper do not necessarily represent the views of the U.S. Department of Energy or the United States Government. This article has been authored by an employee of National Technology & Engineering Solutions of Sandia, LLC under Contract No. DE-NA0003525 with the U.S. Department of Energy (DOE). The employee owns all right, title and interest in and to the article and is solely responsible for its contents. The United States Government retains and the publisher, by accepting the article for publication, acknowledges that the United States Government retains a non-exclusive, paid-up, irrevocable, world-wide license to publish or reproduce the published form of this article or allow others to do so, for United States Government purposes. The DOE will provide public access to these results of federally sponsored research in accordance with the DOE Public Access Plan https://www.energy.gov/downloads/doe-public-access-plan. SAND???. R. Vasconcellos acknowledges the financial support of the Brazilian agency CAPES (grant 88881.302889/2018-01).

Compliance with Ethical Standards

Conflict of Interest: The authors declare that they have no conflicts of interest.

Data Availability Statement: Data will be made available on reasonable request.

References

[1] Chen, L., Zeng, Z., Zhang, D., and Wang, J., 2022, "Vibration Properties of Dual-Rotor Systems under Base Excitation, Mass Unbalance and Gravity," Applied Sciences, **12**(3), 960. Doi: https://doi.org/10.3390/app12030960

[2] Patil, V.R. and Jadhav, P.V., 2020, "Dynamic response analysis of unbalanced rotor-bearing system with internal radial clearance," SN Applied Sciences, **2**(11), 1826. Doi: https://doi.org/10.1007/s42452-020-03608-y

[3] Xu, M., Han, Y., Sun, X., Shao, Y., Gu, F., and Ball, A.D., 2022, "Vibration characteristics and condition monitoring of internal radial clearance within a ball bearing in a gear-shaft-bearing system," Mechanical Systems and Signal Processing, **165**, 108280. Doi: https://doi.org/10.1016/j.ymssp.2021.108280

[4] Craig, W.R.R.J and Kurdila, A.J., Fundamentals of Structural Dynamics, 2nd ed. New York: John Wiley and Sons, 2006.

[5] Nayfeh, A.H., 2008. Perturbation methods, John Wiley & Sons Inc.

[6] Gzal, M., Fang, B., Vakakis, A.F., Bergman, L.A., and Gendelman, O.V., 2020, "Rapid non-resonant intermodal targeted energy transfer (IMTET) caused by vibro-impact nonlinearity," Nonlinear Dynamics, **101**(4), pp. 2087-2106. Doi: https://doi.org/10.1007/s11071-020-05909-8

[7] Shaw, A.D., Hill, T.L., Neild, S.A., and Friswell, M.I., 2016, "Periodic responses of a structure with 3:1 internal resonance," Mechanical Systems and Signal Processing, **81**, pp. 19-34. Doi: https://doi.org/10.1016/j.ymssp.2016.03.008

[8] Detroux, T., Renson, L., Masset, L., Kerschen, G., 2015, "The harmonic balance method for bifurcation analysis of large-scale nonlinear mechanical systems," Computer Methods in Applied Mechanics and Engineering, **296**, pp. 18-38. Doi: https://doi.org/10.1016/j.cma.2015.07.017

[9] Herrera, C.A., McFarland, D.M., Bergman, L.A., and Vakakis, A.F., 2017, "Methodology for nonlinear quantification of a flexible beam with a local, strong nonlinearity," Journal of Sound and Vibration, **388**, pp. 298-314. Doi: https://doi.org/10.1016/j.jsv.2016.10.037

[10] Gzal, M., Vakakis, A.F., Bergman, L.A., and Gendelman, O.V., 2021, "Extreme intermodal energy transfers through vibro-impacts for highly effective and rapid blast mitigation," Communications in Nonlinear Science and Numerical Simulation, **103**, 106012. Doi: https://doi.org/10.1016/j.cnsns.2021.106012

[11] Kuether, R.J., Renson, L., Detroux, T., Grappasonni, C., Kerschen, G., & Allen, M.S., 2015, "Nonlinear normal modes, modal interactions and isolated resonance curves", Journal of Sound and Vibration, **351**, pp. 299-310. Doi: https://doi.org/10.1016/j.jsv.2015.04.035

[12] Ehrich, F.F. and O'Connor, J.J., 1967, "Stator whirl with rotors in bearing clearance," ASME Journal of Engineering for Industry, **89**(3), pp. 381-389. Doi: https://doi.org/10.1115/1.3610057

[13] Baguet, S. and Jacquenot, G., 2010, "Nonlinear couplings in a gear-shaft-bearing system," Mechanism and Machine Theory, **45**(12), pp. 1777-1796. Doi: https://doi.org/10.1016/j.mechmachtheory.2010.08.009

[14] Gunduz, A., Dreyer, J.T., and Singh, R., 2012, "Effect of bearing preloads on the modal characteristics of a shaft-bearing assembly: Experiments on double row angular contact ball

bearings," Mechanical Systems and Signal Processing, **31**, pp. 176-195. Doi: https://doi.org/10.1016/j.ymssp.2012.03.013

[15] Ehehalt, U., Alber, O., Markert, R., and Wegener, G., 2019, "Experimental observations on rotor-to-stator contact," Journal of Sound and Vibration, **446**, pp. 453-467. Doi: https://doi.org/10.1016/j.jsv.2019.01.008

[16] Molaie, M., Samani, F.S., Zippo, A., Pellicano, F., 2022, "Spiral bevel gears: nonlinear dynamic model based on accurate static stiffness evaluation," Journal of Sound and Vibration, In Press, Journal Pre-proof, 117395. Doi: https://doi.org/10.1016/j.jsv.2022.117395.

[17] Chen, Y., Hou, L., Chen, G., Song, H., Lin, R., Jin, Y., and Chen, Y., 2023, "Nonlinear dynamics analysis of a dual-rotor-bearing-casing system based on a modified HB-AFT method," Mechanical Systems and Signal Processing, **185**, 109805. Doi: https://doi.org/10.1016/j.ymssp.2022.109805

[18] Habib, G., Cirillo, G.I., & Kerschen, G., 2018, "Isolated resonances and nonlinear damping," Nonlinear Dynamics, **93**, pp. 979–994. Doi: https://doi.org/10.1007/s11071-018-4240-z

[19] Zhao, G., Paknejad, A., Raze, G., Deraemaeker, A., Kerschen, G., and Collette, C., 2019, "Nonlinear positive position feedback control for mitigation of nonlinear vibrations," Mechanical systems and signal processing, **132**, pp. 457-470. Doi: https://doi.org/10.1016/j.ymssp.2019.07.005

[20] Detroux, T., Noël, J.P., Virgin, L.N., and Kerschen, G., 2018, "Experimental study of isolas in nonlinear systems featuring modal interactions," PLoS ONE, **13**(3), e0194452. Doi: https://doi.org/10.1371/journal.pone.0194452

[21] Renson, L., Shaw, A.D., Barton, D.A., and Neild, S.A., 2019, "Application of control-based continuation to a nonlinear structure with harmonically coupled modes," Mechanical Systems and Signal Processing, **120**, pp. 449-464. Doi: https://doi.org/10.1016/j.ymssp.2018.10.008

[22] Habib, G., Detroux, T., Viguié, R., and Kerschen, G., 2015, "Nonlinear generalization of Den Hartog's equal-peak method," Mechanical Systems and Signal Processing, **52**, pp. 17-28. Doi: https://doi.org/10.1016/j.ymssp.2014.08.009

[23] Hong, D., Hill, T.L., and Neild, S.A., 2019, "Conditions for the existence of isolated backbone curves," Proceedings of the Royal Society A, **475**(2232), 20190374. Doi: https://doi.org/10.1098/rspa.2019.0374

[24] Marchionne, A., Ditlevsen, P., and Wieczorek, S., 2018, "Synchronisation vs. resonance: Isolated resonances in damped nonlinear oscillators," Physica D: Nonlinear Phenomena, **380**, pp. 8-16. Doi: https://doi.org/10.1016/j.physd.2018.05.004

[25] Volvert, M. and Kerschen, G., 2021, "Phase resonance nonlinear modes of mechanical systems," Journal of Sound and Vibration, **511**, p.116355. Doi: https://doi.org/10.1016/j.jsv.2021.116355

[26] Gatti, G., 2016, "Uncovering inner detached resonance curves in coupled oscillators with nonlinearity," Journal of Sound and Vibration, **372**, pp. 239-254. Doi: https://doi.org/10.1016/j.jsv.2016.02.027

[27] Gatti, G. and Brennan, M.J., 2017, "Inner detached frequency response curves: an experimental study," Journal of Sound and Vibration, **396**, pp. 246-254. Doi: https://doi.org/10.1016/j.jsv.2017.02.008

[28] Saunders, B.E., Vasconcellos, R., Kuether, R.J., and Abdelkefi, A., 2021, "Characterization and interaction of geometric and contact/impact nonlinearities in dynamical systems," Mechanical systems and Signal Processing, **167**(A), 108481. Doi: https://doi.org/10.1016/j.ymssp.2021.108481

[29] Nayfeh, A.H. and Balachandran, B., 2008. Applied nonlinear dynamics: analytical, computational, and experimental methods, John Wiley & Sons Inc.

[30] Goldberg, N.N., Demsky, S., Youssef, A.A., Carter, S.P., Fowler, D., Jackson, N., Kuether, R.J., and Steyer, A., "Experimental and computational investigation of nonlinear dynamics of a simplified bearing-and-shaft assembly," 40th International Modal Analysis Conference (IMAC XL), Orlando, FL, February 7-10, 2022.

[31] Wright, J.P. and Pei, J-S, 2012, "Solving Dynamical Systems Involving Piecewise Restoring Force Using State Event Location," Journal of Engineering Mechanics, **138**(8), pp. 997-1020. Doi: https://doi.org/10.1061/(ASCE)EM.1943-7889.0000404

[32] Saunders, B.E., Vasconcellos, R., Kuether, R.J., and Abdelkefi, A., 2021, "Relationship between the contact force strength and numerical inaccuracies in piecewise-smooth systems," International Journal of Mechanical Sciences, **210**, 106729. Doi: https://doi.org/10.1016/j.ijmecsci.2021.106729

[33] Colaïtis, Y. and Batailly, A., "The harmonic balance method with arc-length continuation in blade-tip/casing contact problems," Journal of Sound and Vibration, **502**, p.116070, 2021. Doi: https://doi.org/10.1016/j.jsv.2021.116070

[34] Lazarus, A. and Thomas, O., 2010, "A harmonic-based method for computing the stability of periodic solutions of dynamical systems," Comptes Rendus Mécanique, **338**(9), pp. 510-517. Doi: https://doi.org/10.1016/j.crme.2010.07.020

[35] Saunders, B.E., Vasconcellos, R., Kuether, R.J., and Abdelkefi, A., "Stability and convergence analysis of the harmonic balance method for a Duffing oscillator with freeplay nonlinearity," 40th International Modal Analysis Conference (IMAC XL), Orlando, FL, February 7-10, 2022.

[36] Heinze, T., Panning-von Scheidt, L., & Wallaschek, J., 2020, "Global detection of detached periodic solution branches of friction-damped mechanical systems," Nonlinear Dynamics, **99**, pp. 1841–1870. Doi: https://doi.org/10.1007/s11071-019-05425-4

[37] Vadcard, T., Colaïtis, Y., Batailly, A., and Thouverez, F., 2022, "Assessment of Two Harmonic Balance Method-Based Numerical Strategies for Blade-Tip/Casing Interactions: Application to NASA Rotor 67," Journal of Engineering for Gas Turbines and Power, **144**(12), 121004. Doi: https://doi.org/10.1115/1.4055416

[38] Budd, C. and Dux, F., 1994, "Chattering and related behaviour in impact oscillators," Philosophical Transactions of the Royal Society of London. Series A: Physical and Engineering Sciences, **347**(1683), pp. 365-389. Doi: https://doi.org/10.1098/rsta.1994.0049

[39] Nordmark, A.B. and Piiroinen, P.T., 2009, "Simulation and stability analysis of impacting systems with complete chattering," Nonlinear Dynamics, **58**(1), pp. 85-106. Doi: https://doi.org/10.1007/s11071-008-9463-y

[40] Dankowicz, H. and Fotsch, E., 2017, "On the analysis of chatter in mechanical systems with impacts," Procedia IUTAM, **20**, pp. 18-25. Doi: https://doi.org/10.1016/j.piutam.2017.03.004

[41] Guillot, L., Vigué, P., Vergez, C., and Cochelin, B., 2017, "Continuation of quasi-periodic solutions with two-frequency harmonic balance method," Journal of Sound and Vibration, **394**, pp. 434-450. Doi: https://doi.org/10.1016/j.jsv.2016.12.013

[42] Liao, H., Zhao, Q., and Fang, D., 2020, "The continuation and stability analysis methods for quasi-periodic solutions of nonlinear systems," Nonlinear Dynamics, **100**, pp. 1469–1496. Doi: https://doi.org/10.1007/s11071-020-05497-7

[43] Zheng, Z., Lu, Z.R., Liu, G., and Chen, Y.M., 2022, "Twice harmonic balance method for stability and bifurcation analysis of quasi-periodic responses," Journal of Computational and Nonlinear Dynamics, Paper Number CND-22-1187. Doi: https://doi.org/10.1115/1.4055923